

IMAGE SEGMENTATION BASED ON VARIATIONAL TECHNIQUES

A THESIS SUBMITTED TO
THE GRADUATE SCHOOL OF NATURAL AND APPLIED SCIENCES
OF
THE MIDDLE EAST TECHNICAL UNIVERSITY

BY

ALPER DURAMAZ

IN PARTIAL FULFILLMENT OF THE REQUIREMENTS
FOR
THE DEGREE OF MASTER OF SCIENCE
IN
ELECTRICAL AND ELECTRONICS ENGINEERING

SEPTEMBER 2006

Approval of the Graduate School of Natural and Applied Sciences

Prof. Dr. Canan ÖZGEN
Director

I certify that this thesis satisfies all the requirements as a thesis for the degree of Master of Science.

Prof. Dr. İsmet ERKMEN
Head of Department

This is to certify that we have read this thesis and that in our opinion it is fully adequate, in scope and quality, as a thesis for the degree of Master of Science.

Prof. Dr. Kemal LEBLEBİCİOĞLU
Co-advisor

Prof. Dr. Zafer ÜNVER
Supervisor

Examining Committee Members

Prof. Dr. Uğur HALICI	(METU, EEE)	_____
Prof. Dr. Zafer ÜNVER	(METU, EEE)	_____
Prof. Dr. Kemal LEBLEBİCİOĞLU	(METU, EEE)	_____
Assoc. Prof. Dr. Gözde BOZDAĞI AKAR	(METU, EEE)	_____
Umur AKINCI (M.S.)	(ASELSAN, MGEO)	_____

I hereby declare that all information in this document has been obtained and presented in accordance with academic rules and ethical conduct. I also declare that, as required, I have fully cited and referenced all material and results that are not original to this work.

Name Lastname : Alper DURAMAZ

Signature :

ABSTRACT

IMAGE SEGMENTATION BASED ON VARIATIONAL TECHNIQUES

DURAMAZ, Alper

M.Sc., Department of Electrical and Electronics Engineering

Supervisor: Prof. Dr. Zafer ÜNVER

Co-Supervisor: Prof. Dr. Kemal LEBLEBİCİOĞLU

September 2006, 88 pages

Recently, solutions to the problem of image segmentation and denoising are developed based on the Mumford-Shah model. The model provides an energy functional, called the Mumford-Shah functional, which should be minimized. Since the minimization of the functional has some difficulties, approximate approaches are proposed. Two such methods are the gradient flows method and the Chan-Vese active contour method. The performance evolution in terms of speed shows that the gradient flows method converges to the boundaries of the smooth parts faster; but for the hierarchical four-phase segmentation, it is observed that this method sometimes gives unsatisfactory results. In this work, a fast hierarchical four-phase segmentation method is proposed where the Chan-Vese active contour method is applied following the gradient flows method. After the segmentation process, the segmented regions are denoised using diffusion filters. Additionally, for the low signal-to-noise ratio applications, the prefiltering scheme using nonlinear diffusion filters is included in the proposed method. Simulations have shown that the proposed method provides an effective solution to the image segmentation and denoising problem.

Keywords: Mumford-Shah functional, image segmentation, denoising, level set methods, diffusion filters

ÖZ

DEĞİŞİMSEL TEKNİKLERE DAYALI GÖRÜNTÜ AYRIŞTIRMA

DURAMAZ, Alper

Yüksek Lisans, Elektrik ve Elektronik Mühendisliği Bölümü

Tez Yöneticisi: Prof. Dr. Zafer ÜNVER

Ortak Tez Yöneticisi: Prof. Dr. Kemal LEBLEBİCİOĞLU

Eylül 2006, 88 sayfa

Son zamanlarda görüntüyü ayrıştırma ve gürültüden temizleme problemi için Mumford-Shah modelini temel alan çözümler geliştirilmiştir. Bu model Mumford-Shah fonksiyoneli olarak adlandırılan ve enazlanması gereken bir enerji fonksiyoneli sağlamaktadır. Bu fonksiyonelin enazlanmasındaki bazı zorluklardan ötürü bazı yaklaşık yöntemler önerilmiştir. Bu yöntemlerden ikisi gradyan akışlar ve Chan-Vese etkin çevre hatları yöntemleridir. Yöntemlerin hız bakımından başarımlarını değerlendirilmesi, gradyan akışlar yönteminin görüntünün düzgün kısımlarına ait sınırları daha çabuk yakınsadığını göstermiştir. Ancak dört evreli hiyerarşik ayrıştırma durumlarında, gradyan akışlar yönteminin bazen yetersiz sonuçlar verdiği gözlemlenmiştir. Bu çalışmada, gradyan akışlar yöntemi ardından Chan-Vese etkin çevre hatları yönteminin kullanıldığı hızlı bir dört evreli hiyerarşik ayrıştırma yöntemi önerilmiştir. Ayrıştırma işleminin ardından, gürültüden arındırma işlemi ayrıştırılan alanlarda difüzyon süzgeçleri kullanılarak yapılmıştır. Ek olarak, işaret/gürültü oranının düşük olduğu uygulamalarda, doğrusal olmayan difüzyon süzgeçlerinin kullanıldığı ön süzgeçleme işlemi önerilen yönteme eklenmiştir. Benzetim çalışmaları, önerilen yöntemin görüntüyü ayrıştırma ve gürültüden temizleme problemine etkin bir çözüm getirdiğini göstermiştir.

Anahtar sözcükler: Mumford-Shah fonksiyoneli, görüntü ayrıştırma, gürültüden arındırma, seviye kümesi yöntemleri, difüzyon süzgeçler

To My Beloved Işın and My Family

ACKNOWLEDGMENTS

I would like to express my sincere gratitude to my supervisor Prof. Dr. Zafer ÜNVER and my co-supervisor Prof. Dr. Kemal LEBLEBİCİOĞLU for their supervision, guidance and encouragement throughout this study.

Special thanks to my beloved girlfriend Işın and my little brother Caner for their help during the preparation of the thesis and extraordinary patience through this duration. They are the stubborn supporters who do not give up assisting me. I am grateful to Zeynep for her nice drawings in the thesis.

I am forever indebted to my parents who have been supporting me in every aspects of life.

I would like to extend my appreciation to my friends, my colleagues for their valuable support and fellowship.

Thanks to all esteemed people who refine my life style.

TABLE OF CONTENTS

PLAGIARISM	iii
ABSTRACT	iv
ÖZ	vi
ACKNOWLEDGEMENTS	ix
TABLE OF CONTENTS	x
CHAPTER	
1 INTRODUCTION	1
2 PRELIMINARIES	5
2.1 Level Set Methods	5
2.2 Gradient Flows	9
2.2.1 Gradient Flow Minimizing the Arc-Length of a Closed Curve	9
2.2.2 Gradient Flow Minimizing Region Integrals	10
2.3 Diffusion Filtering Techniques	11
3 THE PROPOSED IMAGE SEGMENTATION AND DENOISING	
METHOD	14
3.1 The Mumford-Shah Model	14
3.2 Fundamentals of the Proposed Method	18
3.2.1 Active Contours without Edges	19
3.2.2 Approximated Mumford-Shah Flow	33
3.2.3 Four-Phase Hierarchical Image Segmentation	36

3.2.4	Denoising After Segmentation	49
3.2.5	Effects of Prefiltering	57
3.3	Proposed Method	60
3.4	Comparison of the Proposed Method with the Normalized Cuts Method	60
4	SIMULATIONS ON SOME APPLICATIONS	65
4.1	Simulations on Medical Imagery	65
4.2	Simulations on Thermal Imaging	68
4.3	Simulations on SAR Imagery	70
5	CONCLUSION	74
APPENDICES		
A	FIRST VARIATION AND EULER-LAGRANGE EQUATION ..	77
B	CURVATURE	80
B.1	Curvature of the Parameterized Curves	80
B.2	Curvature of the Curves as Isolevels of a Function	81
C	FLUX MAXIMIZING FLOW	83
REFERENCES	85

LIST OF FIGURES

2.1	The intersection of the higher dimensional evolving surface with the image data plane defines the evolving curve on the image plane.	6
2.2	Unit curve evolution in the gradient direction via level set method. Left: Zero levels of the level set function $\phi(x, y, t)$. Right: $\phi(x, y, 0)$ and $\phi(x, y, 1)$.	8
2.3	(a) A closed curve is placed in a 2D vector field. (b) The curve evolves in order to increase the total inward flux through it. The total inward flux is maximum when the normal vectors of the curve are aligned with the direction of vector field.	12
3.1	A simple image composed of two various open subsets.	16
3.2	The separated homogeneous regions and the corresponding ϕ values in these regions.	24
3.3	The evolution of the curve on the synthetic image (left column) and the corresponding evolution of the level set function for the Chan-Vese active contour method (right column).	26
3.4	Two different approximations of (a) the Heaviside function and (b) the delta Dirac function.	28
3.5	Segmentation results of the Chan-Vese active contour method with respect to different initial conditions. The first and the second columns show the initial curves on the 100 x 100 synthetic image and the corresponding level set function ϕ_0 . The third column is the final level set function ϕ and (p) is the segmentation result of the different initial conditions. $\mu = 0.01 \times 255^2$, $\lambda = 10$.	29
3.6	The detection of the interior boundary of the objects when the initial zero level of ϕ is outside the outer boundary.	32

3.7	Segmentation of noisy images by the Chan-Vese active contours method. (a) 120 x 201 synthetic image with zero mean Gaussian white noise (SNR = 20dB). (b) Segmented synthetic image. $\mu = 2\sigma^2 = 3994$, $\lambda = 6$. Computation time is 83 s. (c) 300 x 196 burning candle image with zero mean Gaussian white noise (SNR = 10dB). (d) Segmented burning candle image. $\mu = 2\sigma^2 = 3798$, $\lambda = 6$. Computation time is 547.4 s.	34
3.8	The evolution of the curve on the hand image (left column) and the corresponding evolution of the level set function for the approximate Mumford-Shah gradient flow method (right column).	37
3.9	Segmentation results of the approximate Mumford-Shah gradient flow with respect to different initial conditions. The first and the second columns show the initial curves on the 100 x 100 hand image and the corresponding level set function ϕ_0 . The third column is the final level set function ϕ and (p) is the segmentation result of the different initial conditions. $\mu = 0.0001 \times 255^2$, $\lambda = 1$)	39
3.10	Segmentation of noisy images by the approximate Mumford-Shah gradient flow method. $\mu = 0.0001 \times 255^2$, $\lambda = 1$. (a) 120 x 201 synthetic image with zero mean Gaussian white noise (SNR = 20dB). (b) Segmented synthetic image. Computation time is 3.2 s. (c) 300 x 196 burning candle image with zero mean Gaussian white noise (SNR = 10dB). (d) Segmented burning candle image. Computation time is 4.3 s.	41
3.11	An image where two smooth regions with comparable mean values are one inside the other.	42
3.12	(a) Two level set functions, ϕ_1 and ϕ_2 , partition the image domain into four regions. (b) Three level set functions, ϕ_1 , ϕ_2 and ϕ_3 , partition the image domain into eight regions.	43

3.13	The hierarchical four-phase segmentation based on the Chan-Vese active contour method. Image size: 120 x 201, $\mu_1 = \mu_2 = 0.0001 \times 255^2$, $\lambda_1 = \lambda_2 = 1$. (a) The synthetic image composed of three regions with two different mean values and the initial curves. (b) Segmentation result of (a). Computation time is 6.8 s. (c) The synthetic image composed of three regions with three different mean values and the initial curves belonging to the first step. (d) Segmentation result of the first step. Computation time is 14.4 s. (e) The initial curves belonging to the second step. (f) Segmentation result of the second step. Total computation time is 684.2 s.	46
3.14	The hierarchical four-phase segmentation based on the approximate Mumford-Shah gradient flow method. Image size: 64 x 64, $\mu_1 = \mu_2 = 0.0001 \times 255^2$, $\lambda_1 = \lambda_2 = 1$. (a) The synthetic image composed of three regions with two different mean values and the initial curves. (b) Segmentation result of (a). Computation time is 0.8 s. (c) The synthetic image composed of three regions with three different mean values and the initial curves belonging to the first step. (d) Segmentation result of the first step. Computation time is 0.6 s. (e) The initial curves belonging to the second step. (f) Segmentation result of the second step. Total computation time is 1.1 s.	48
3.15	The hierarchical four-phase segmentation based on the approximate Mumford-Shah gradient flow method without the detection of the object boundary. Image size: 120 x 201, $\mu_1 = \mu_2 = 0.0001 \times 255^2$, $\lambda_1 = \lambda_2 = 1$	50
3.16	The hierarchical four-phase segmentation based on the approximate Mumford-Shah gradient flow method with the detection of the small variations in the homogeneous regions. Image size: 120 x 201, $\mu_1 = \mu_2 = 0.0001 \times 255^2$, $\lambda_1 = \lambda_2 = 100000$	51

- 3.17 The hierarchical four-phase segmentations based on the Chan-Vese active contour method (left column) and the proposed method (right column). (a) 64 x 64 synthetic image with zero mean Gaussian white noise (SNR = 25dB) and the initial curves for the first step (b), (c) The results of the first steps. (b) $\mu_1 = 0.5\sigma^2 = 1484$, $\lambda_1 = 6$, (c) $\mu_1 = 0.0001 \times 255^2$, $\lambda_1 = 1$. Computation times are (b) 27.8 s, (c) 0.8 s. (d), (e) The initial curves for the second steps. (f), (g) The results of the second steps. $\mu_2 = 0.5\sigma^2 = 1484$, $\lambda_2 = 6$. Total computation times are (f) 43.7 s, (g) 12.5 s. 52
- 3.18 Segmentation of the well-known house image using the proposed hierarchical four-phase segmentation approach. (a) The original 256 x 256 test image. (b) The segmented image after the first segmentation step. $\mu_1 = 0.0001 \times 255^2$, $\lambda_1 = 1$. Computation time is 4.7 s. (c) The segmented image after the second segmentation step. $\mu_2 = 0.5\sigma^2 = 1059$, $\lambda_2 = 6$. Total computation time is 667.9 s. 54
- 3.19 Over-segmentation of an image. (a) The original 126 x 87 test image. (b) The segmented image after the first segmentation step. $\mu_1 = 0.0001 \times 255^2$, $\lambda_1 = 1$. Computation time is 0.8 s. (c) The segmented image after the second segmentation step. $\mu_2 = 0.5\sigma^2 = 502.2$, $\lambda_2 = 6$. Total computation time is 53.3 s. 55
- 3.20 The effect of the anisotropic diffusion filtering on the previously segmented images. Left: The segmented noisy images. (a) Natural noise. The input SNRs are (c) 10 dB, (e) 25 dB. Right: Filtered images. The output SNRs are (d) 17.45 dB, (f) 35.55 dB. 56
- 3.21 The effect of the prefiltering scheme for the segmentation and denoising of the very noisy images. The First Row: The original images with white Gaussian noise. The input SNRs are (a) 3 dB, (b) 13 dB. The Second Row: The unsatisfactory segmentations. The Third Row: The smoothed images after prefiltering. The Last Row: The filtered images after segmentation and denoising. The output SNRs are (g) 11.46 dB, (h) 23.1 dB. 58

3.22	The segmentation results due to the proposed method (left column) and the normalized cuts method (right column). The corresponding computation times are (a) 2 s, (b) 28.3 s, (c) 0.4 s, (d) 10.8 s, (e) 0.4 s (f) 12.9 s, (g) 12.5 s, (h) 2.7s, (i) 0.4 s, (j) 15.7 s, (k) 401 s, (l) 77 s. The number of segments set at the beginning in the normalized cuts method are (b) 4, (d) 2, (f) 3, (h) 6, (j) 5 and (l) 20.	62
4.1	The segmentation and denoising of MRI images with the proposed method. Prefiltering scheme is not applied. (a), (d), (g) Original MRI images. (a) Image size: 256 x 192. (d) Image size: 182 x 182. (g) Image size: 182 x 182. (b), (e), (h) The segmented parts in the images. Computation times are (b) 212.7 s, (e) 217.2 s and (h) 103.9 s. (c), (f), (i) Filtered MRI images.	66
4.2	The segmentation and denoising of infrared images with the proposed method. Prefiltering scheme is not applied. (a), (b) Original infrared images. (a) Image size: 80 x 166. (b) Image size: 89 x 120. (c), (d) The segmented parts in the images. (c) Only one level set function is applied. Computation times are (c) 1.6 s and (d) 14.1 s. (e), (f) Filtered infrared images.	69
4.3	The segmentation and denoising of SAR images with the proposed method. (a), (b) Original SAR images. Image size: 128 x 128 (c), (d) The denoised images after prefiltering. (e), (f) The segmented parts in the images. Computation times are (e) 34.2 s and (f) 30.1 s. (g), (h) Filtered SAR images.	72
B.1	Curvature of a curve.	81

CHAPTER 1

INTRODUCTION

The issue of segmenting and denoising a noisy image is inevitable for the applications where the details of the image is required, e.g., satellite imaging, astronomical imaging, medical imaging, video processing, robot vision, oceanography and radar applications. It can be applicable for any case in which the objects in an image has to be identified with distinguishing parameters such as edges, holes, etc.

In order to solve the problem, variational based image segmentation and partial differential equation (PDE) based image smoothing approaches have been developed. The methods for the former include snakes based on the gradient [9], geodesic active contours [3], curve evolution based on the Mumford-Shah variational model [22] and active contours without edges [5]. The simple idea behind these methods is that an initial curve evolves according to image statistics inside and outside it and stops evolving at the boundaries of objects according to a stopping criterion, e.g., high magnitude of the gradient vectors. For the latter, the anisotropic diffusion and the nonlinear diffusion models introduced by Perona and Malik [14] are popular. These models basically detect the boundaries among the smooth (homogeneous) regions and filter the regions independently. Filtering does not take place at the boundaries in order not to loose the boundary information.

In the late 80s, Mumford and Shah have developed a variational based image segmentation and denoising scheme [10]. This model became one of the most widely studied mathematical models that enables simultaneous denoising and smoothing of a noisy image. The main idea is to minimize the energy functional, known as the Mumford-Shah functional, in order to obtain the homogeneous representation of the image and detect the boundaries of the smooth regions.

The minimization of the Mumford-Shah functional is not an easy task due to the dependency on its variables. Thus, the approximate minimization approach is followed where one of the variables is fixed and the energy functional is minimized with respect to the other variable. Finally, a set of weak Poisson equations for the smooth representation of the image and the curve evolution equation for the segmenting closed curves, known as the Mumford-Shah gradient flow, are obtained.

After Mumford and Shah proposed their model, the minimization of their functional is considered to be an attractive issue because of its high segmenting and smoothing capability. It is investigated in both stochastic and deterministic manners. Schneider and Fieguth have developed a Bayesian interpretation of the revised Mumford-Shah approach [17]. In their variational model, the piecewise smooth output image and the edge strength function which has the same dimensions with the noisy image are introduced as variables. The edge-strength function takes the values between 0 and 1. It is approximately 0 in the smooth regions of the image and very close to 1 at the boundaries. The outcoming model equations have close relationship with the Kalman filtering equations.

However, majority of the researches have paid attention to the numerical implementation of minimizing the Mumford-Shah functional from the deterministic point of view. First practical implementations are achieved by Richardson [15] working on the elliptic approximation of the Mumford-Shah functional developed by Ambrossio and Tortorelli [2]. Recently, Chan and Vese dealt with the problem using the active contours without edges [5], [24]. Meanwhile, Tsai developed the simultaneous curve evolution based segmenting and the PDE based smoothing framework [22] using the results obtained in [10]. In his framework, Tsai has introduced multiresolution segmentation and noticed on some applications of his approach such as blockiness image magnification and reconstruction of images with missing data. Gao and Bui have mentioned the disadvantages of PDE based smoothing schemes such as high computation time and low denoising capability [8]. They have used the method of active contours without edges for the segmentation problem and pointed that the smoothing via any of the diffusion filtering methods is adequate after the segmentation of the image.

The efficiency of the Chan-Vese active contour method has been increased by using the simultaneous and the hierarchical multiphase segmentation approaches in the sense of getting more details of the objects in [24] and [8], respectively.

Chan and Vese approximated the Mumford-Shah energy functional by its piecewise constant representation and reformulated it by the level set methods introduced in [18]. Minimizing the modified form of the energy functional, a PDE relating to a surface evolution which depends on the image characteristics is obtained. The zero level of the evolving surface is a moving curve in order to segment the homogeneous parts in the image. By the help of surface evolution, the segmentation process is speeded up significantly and also the interior contours of the objects are detected. Similarly, Tsai embedded a level set function to the Mumford-Shah gradient flow.

In this work, the segmentation and denoising problem is handled with a similar step order proposed by Gao and Bui. In order to select which type of segmentation algorithm is to be used, the Chan-Vese active contour method and the piecewise constant approximation of the Mumford-Shah gradient flow method in [22] are investigated. Since the resulting minimizer of the Mumford-Shah gradient flow uses the whole image plane for the surface evolution rather than using a part of it, it results in a faster convergence to the object boundaries. Unfortunately, in some simulations for the hierarchical multiphase segmentation, it is observed that the method yields unsatisfactory results such as detecting the small variations inside the smooth regions. Depending on these observations, the approximated hierarchical four-phase segmentation approach proposed in this work is formed by activating the Chan-Vese active contour method after the approximated Mumford-Shah gradient flow method in case the latter does not satisfy the expectations in the first step of the segmentation process. Once, the segmentation finishes, anisotropic diffusion filtering is applied in the segmented regions independently. This segmentation and denoising methodology is not working properly for the applications where the signal level is low as compared to the noise. In order to overcome this problem, a prefiltering scheme is added to the algorithm. Nonlinear diffusion filtering is selected as the type of prefilter, because it does not smooth the edges while smoothing the interior regions.

The work is organized as follows. In Chapter 2, some preliminary knowledge on level set methods, gradient flows and diffusion filters are presented. In Chapter 3, the Mumford-Shah functional is analyzed and the results obtained by minimizing the functional are given. The Chan-Vese active contour method and the level set formulation of the approximated Mumford-Shah gradient flow are explained and comparisons, in the sense of speed of convergence and relevancy of the segmentation results, are made. Then, the steps to be followed in the segmenting and denoising algorithm are elucidated. In Chapter 4, the algorithm is attempted on medical imagery, thermal imaging and SAR imagery. Finally, in Chapter 5 the conclusions are provided.

CHAPTER 2

PRELIMINARIES

In this chapter, the level set methods, the gradient flows and the diffusion filters are explained in order to make an explicit investigation of the previously proposed algorithms in the subsequent chapters.

2.1 Level Set Methods

Classical snakes based algorithms or active contours can be used in order to segment objects automatically. The central idea of these algorithms is the evolution of a curve due to the speed function depending on the image and the curve itself until the curve detects the boundary of the objects. The curve evolution stops according to a stopping criterion such as the high magnitude of the image gradient. Since the speed and the stopping functions highly depend on the image data around the evolving curve in each evolution step, the whole image data can not effect the evolution, i.e., the evolution is not globally effected. Therefore, the interior boundaries of the objects such as a ring can not be detected by these algorithms when the initial curve is outside the outermost boundary of the object. Another disadvantage of these algorithms is that the stopping function which depend on the image topology should be defined properly in order not to miss the object boundary.

An approach to overcome these difficulties was first introduced by Sethian and Osher [11], namely the level set methods. In these methods, the evolving curve is modeled as the zero level of a higher dimensional evolving surface, and it can be considered as the intersection of the surface with the image data plane, (see Figure 2.1).

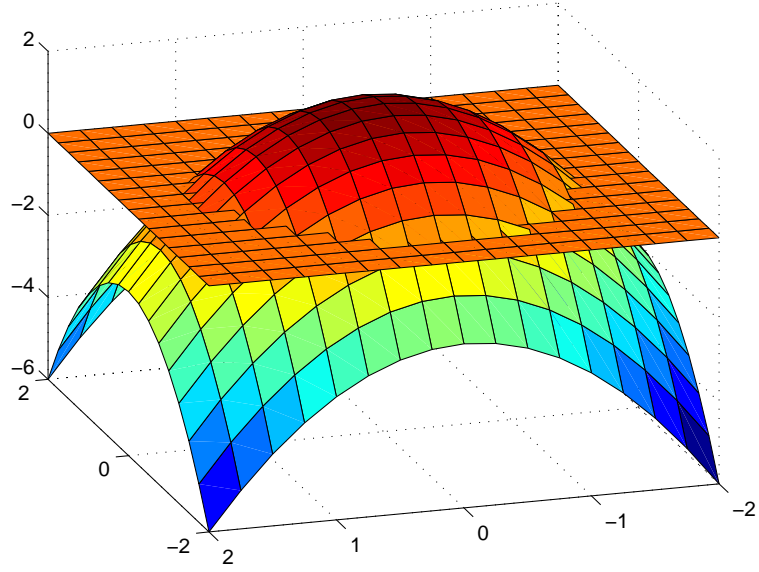


Figure 2.1: The intersection of the higher dimensional evolving surface with the image data plane defines the evolving curve on the image plane.

Let Ω be a bounded open subset of \mathbb{R}^2 , with $\partial\Omega$ as its boundary. Then, a two dimensional image g can be defined as a mapping from Ω into \mathbb{R} , i.e., $g : \Omega \rightarrow \mathbb{R}$. $\vec{C}(t)$ is an evolving curve in Ω , which is the boundary of a bounded open subset ω , i.e., $\omega \subseteq \Omega$, and $\vec{C}(t) = \partial\omega$. The Lipschitz continuous level set function $\phi(x, y, t)$ is defined as a mapping from $\Omega \times \mathcal{T}$ into \mathbb{R} where \mathcal{T} is the time domain, i.e., $\phi(x, y, t) : \Omega \times \mathcal{T} \rightarrow \mathbb{R}$. By Lipschitz continuity, the smoothness of the level set function $\phi(x, y, t)$ is well guaranteed.

As explained before, the evolving curve is modeled as the zero level of $\phi(x, y, t)$. The function is defined such that it is positive (negative) if the point (x, y) is inside (outside) the subset ω , i.e.,

$$\begin{aligned}
 \phi(x, y, t) &> 0 && \text{for } (x, y) \text{ inside } \omega, \\
 \phi(x, y, t) &< 0 && \text{for } (x, y) \text{ outside } \omega, \\
 \phi(x, y, t) &= 0 && \text{for } (x, y) \text{ on } \partial\omega = \vec{C}(t).
 \end{aligned} \tag{2.1}$$

The aim is to find an equation for the evolution of the zero level of $\phi(x, y, t)$ in order to make the zero level converge to the object boundary. The basic evolution equation is given by

$$\frac{\partial\phi}{\partial t} + v \cdot \nabla\phi = 0 \quad (2.2)$$

where $\phi(x, y, 0) = \phi_o(x, y)$ is the initial level set function and v is the velocity field, or informally the directional speed function of the evolving surface. Since the normal component of v is

$$v_N = v \cdot \frac{\nabla\phi}{|\nabla\phi|}, \quad (2.3)$$

the resulting curve evolution level set equation becomes

$$\frac{\partial\phi}{\partial t} + v_N \cdot |\nabla\phi| = 0. \quad (2.4)$$

The velocity field can take several forms. It can be considered as the globally effective counterpart of both the speed and the stopping functions of the curve evolution in the snake based algorithms. Taking $v_N \equiv 1$, the equation (2.4) becomes unit evolution in gradient direction, and the zero level set $\vec{C}(t > 0)$ and the starting zero level set $\vec{C}(t = 0)$ have a positive distance of magnitude t in between assuming they are on the same plane (see Figure 2.2). Another fundamental curve evolution equation defined by a level set function is

$$\frac{\partial\phi}{\partial t} = |\nabla\phi| \operatorname{div} \left(\frac{\nabla\phi}{|\nabla\phi|} \right) - |\nabla\phi| \quad (2.5)$$

where the first part on the right is the mean curvature motion minimizing the length of \vec{C} , and the second part on the right is the constant speed motion minimizing the area inside \vec{C} .

Level set methods are advantageous since they solve the problems encountered in classical snake based algorithms. Another advantage of level set methods is that the geometric properties of the evolving curve are easily determined from a particular level set of $\phi(x, y, t)$.

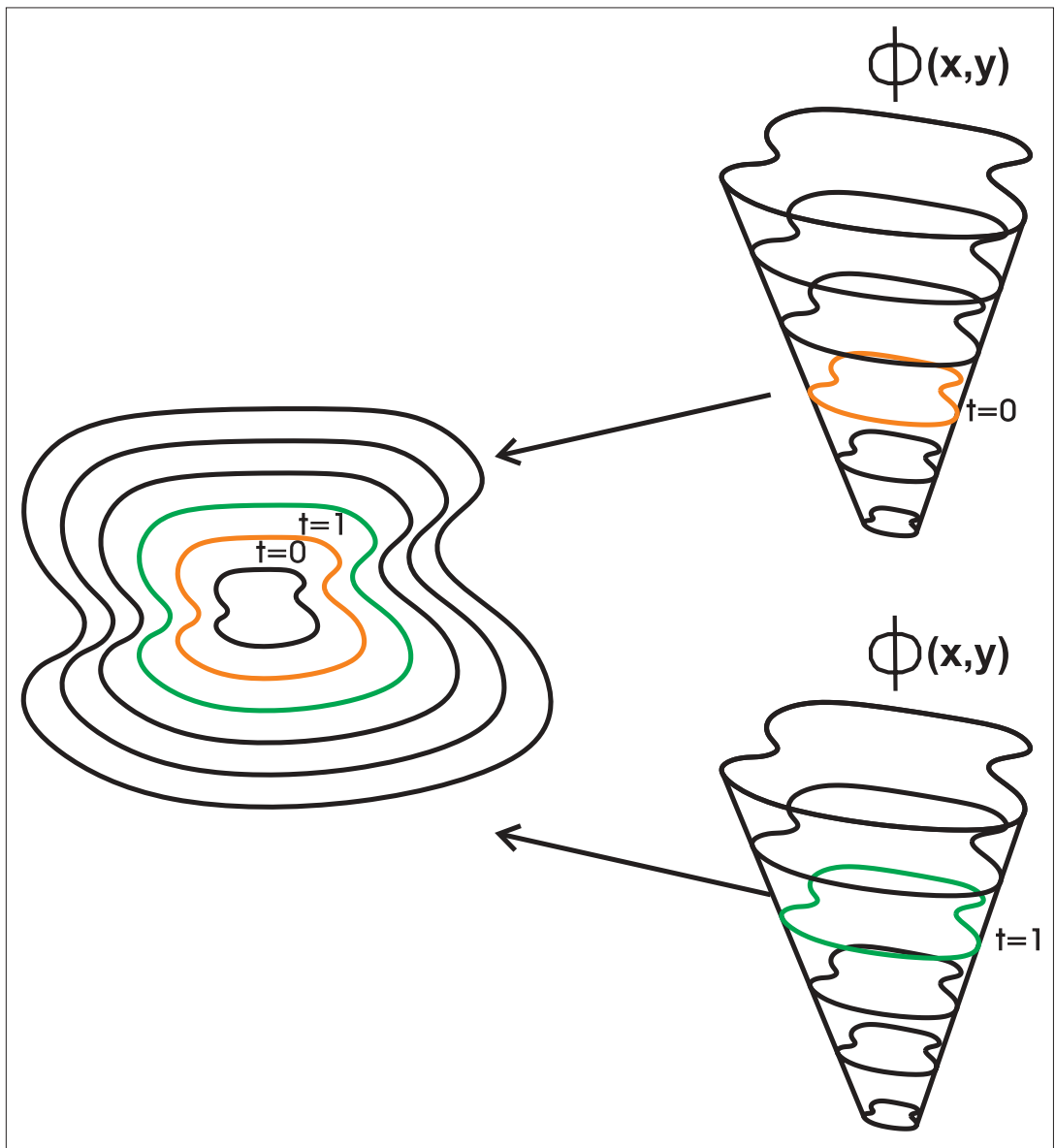


Figure 2.2: Unit curve evolution in the gradient direction via level set method. Left: Zero levels of the level set function $\phi(x, y, t)$. Right: $\phi(x, y, 0)$ and $\phi(x, y, 1)$.

2.2 Gradient Flows

2.2.1 Gradient Flow Minimizing the Arc-Length of a Closed Curve

This method is also known as the Euclidean curve shortening flow in literature. Let $\vec{C}(p, t)$ be a smooth closed curve where $0 \leq p \leq 1$ and t indicates that \vec{C} is time varying. Since the curve is closed and smooth, $\vec{C}(0, t) = \vec{C}(1, t)$ and $\frac{\partial \vec{C}}{\partial t}(p, t)|_{p=0} = \frac{\partial \vec{C}}{\partial t}(p, t)|_{p=1}$. The curve length is calculated by

$$L(t) = \int_0^1 \left\| \frac{\partial \vec{C}}{\partial p} \right\| dp. \quad (2.6)$$

Taking the first variation of (2.6) and integrating by parts

$$\begin{aligned} L'(t) &= \int_0^1 \frac{\left\langle \frac{\partial \vec{C}}{\partial p}, \frac{\partial^2 \vec{C}}{\partial p \partial t} \right\rangle}{\left\| \frac{\partial \vec{C}}{\partial p} \right\|} dp \\ &= \left\langle \frac{\frac{\partial \vec{C}}{\partial p}}{\left\| \frac{\partial \vec{C}}{\partial p} \right\|}, \frac{\partial^2 \vec{C}}{\partial p \partial t} \right\rangle \Big|_0^1 - \int_0^1 \left\langle \frac{\partial \vec{C}}{\partial t}, \frac{1}{\left\| \frac{\partial \vec{C}}{\partial p} \right\|} \frac{\partial}{\partial p} \left[\frac{\frac{\partial \vec{C}}{\partial p}}{\left\| \frac{\partial \vec{C}}{\partial p} \right\|} \right] \left\| \frac{\partial \vec{C}}{\partial p} \right\| \right\rangle dp \end{aligned} \quad (2.7)$$

is obtained. The first term in (2.7) diminishes according to the equality in the first derivative of the curve at the starting and ending points. Parameterizing of the second part of (2.7) with the arc-length

$$ds = \left\| \frac{\partial \vec{C}}{\partial p} \right\| dp \quad (2.8)$$

and using the curvature definition obtained in Appendix B, (2.7) takes its final form

$$L'(t) = - \int_0^{L(t)} \left\langle \frac{\partial \vec{C}}{\partial t}, \kappa \vec{N} \right\rangle ds \quad (2.9)$$

where \vec{N} is the inward normal vector and κ is the curvature of \vec{C} . Thus, the length of curve $\vec{C}(p, t)$ decreases most rapidly when

$$\frac{\partial \vec{C}}{\partial t} = \kappa \vec{N}. \quad (2.10)$$

Conversely, it increases most rapidly in the direction of the outward normal vector. Equation (2.10) is the same with the starting equation used to define the curvature of a curve given in Appendix B.

As a result, the closed curves evolve according to the turning speed vector of their tangential vectors in order to minimize the arc-length. Unless these curves come across with a stopping criterion, they merge to a circle. This result is applied in many active contour methods.

2.2.2 Gradient Flow Minimizing Region Integrals

The purpose of this method is to find the curve evolution which minimizes a double integral \mathcal{K} whose integrand is a continuous scalar field $\mathcal{H} : \mathbb{R}^2 \rightarrow \mathbb{R}$. The region of computation Ω of the double integral is inside the evolving curve \vec{C} .

$$\mathcal{K} = \iint_{\Omega(\vec{C})} \mathcal{H} dA \quad (2.11)$$

The preliminary conditions on \vec{C} stated in the previous section are also valid for this gradient flow.

In order to determine the first variation of \mathcal{K} over the space of closed curves, the scalar field \mathcal{H} can be written as the divergence of a vector field \vec{F} ,

$$\nabla \cdot \vec{F} = \mathcal{H}. \quad (2.12)$$

By the substitution of (2.12), (2.11) is rewritten as

$$\mathcal{K} = \iint_{\Omega(\vec{C})} \nabla \cdot \vec{F} dA. \quad (2.13)$$

Using the divergence theorem, the double integral changes to a line integral. In addition to that, \mathcal{K} varies with t as the curve $\vec{C}(p, t)$ evolves. Then the new form of (2.13) is obtained as

$$\mathcal{K}(t) = \oint_{\vec{C}} \langle \vec{F}, \vec{N} \rangle ds \quad (2.14)$$

where \vec{N} is the inward normal vector. This equation represents the total inward flux through a region enclosed by the curve \vec{C} . Thus, the problem to find

the rate of change of a curve maximizing the double integral in (2.13) is restated as to find the rate of change of a curve minimizing the total inward flux through it. Performing all the necessary computation steps given in Appendix C, [23], [21], the resulting curve equation ends up with

$$\begin{aligned}\vec{C}_t &= (\nabla \cdot \vec{F}) \vec{N} \\ &= \mathcal{H} \vec{N}.\end{aligned}\tag{2.15}$$

From (2.15), it is concluded that the the result of the double integrals whose region of computation depends on an evolving curve is minimized when the curve evolves in its inward normal direction with the magnitude of the scalar field inside it (see Figure 2.3).

2.3 Diffusion Filtering Techniques

Diffusion filtering techniques are PDE-based filtering schemes, and they are widely used for edge preserved smoothing and denoising applications. The algorithms are developed in an iterative manner where the previous output of the filter is the initial condition for the next iteration. If the output of each filtering level is considered as the scale, the smoothness is improving going from the coarser scale to the finer scale. Each scale is defined by the value which is obtained from time varying image function $g(x, y, t)$ at a specific time t . The initial condition for the algorithms is $g(x, y, t = 0) = g_0(x, y)$ where $g_0(x, y)$ is the noisy input image.

The general formulation for the diffusion filters is

$$\frac{\partial g}{\partial t} = \text{div}(\mathcal{D} \nabla g)\tag{2.16}$$

where \mathcal{D} is a scalar function known as the diffusivity term. All diffusion filters are varied according to the different diffusivities.

For the linear isotropic diffusion filtering, the diffusivity is taken as a constant. As a result, (2.16) simplifies to

$$\frac{\partial g}{\partial t} = \mathcal{D} \nabla^2 g.\tag{2.17}$$

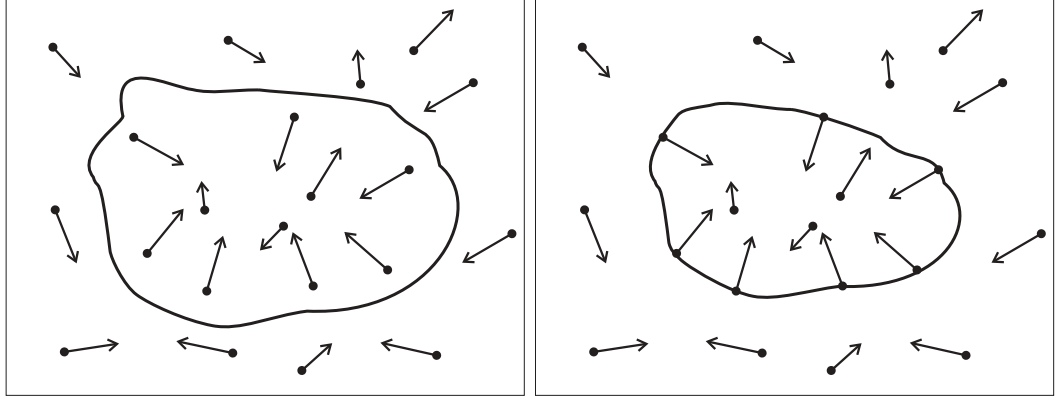


Figure 2.3: (a) A closed curve is placed in a 2D vector field. (b) The curve evolves in order to increase the total inward flux through it. The total inward flux is maximum when the normal vectors of the curve are aligned with the direction of vector field.

Linear isotropic diffusion filters not only smooth the noisy image but also blur the edges, unfortunately.

In order to overcome the edge-blurring defect, the edge-preserving nonlinear isotropic diffusion filtering is developed. The diffusivity function f depends on the increase in the gradient of the filtered $g(x, y, t)$, i.e.,

$$\mathcal{D} = f(|\nabla g_\sigma|) \quad (2.18)$$

where

$$g_\sigma \equiv K_\sigma * g. \quad (2.19)$$

The condition on f is that it is a monotonically decreasing function where $f(0) = 1$ and $f(s) = 0$ for $s \rightarrow \infty$. K_σ is the gaussian filter smoothing the previous scale in order to enable the edge detector, $|\nabla g_\sigma|$, distinguish the edge locations from noise spikes. When the edge detector value is very large, the diffusion does not hold. As a conclusion, the nonlinear isotropic diffusion filter smooths the image, but it is not capable of removing the noise at the edges.

Among all the diffusion filters, the anisotropic diffusion filters result in the highest performance in terms of the preservation of the edges and the denoising

in the regions. It is a special type of nonlinear isotropic diffusion filters and first introduced in [14]; the further developments are given in [1] and [4].

The diffusivity of this type of diffusion filter is formed by taking into account not only the magnitude of the gradient of the gaussian filtered image $|\nabla g_\sigma|$ but also the direction of the gradient vector. The construction of the diffusivity is varying according to the type of application where the anisotropic diffusion is needed. In [25], [26] and [27], Weickert introduced two different anisotropic diffusion filters, namely the edge-enhancing and the coherence-enhancing anisotropic diffusion filters.

The main advantage of anisotropic diffusion to general nonlinear diffusion is that the smoothing takes place in the regions and on the boundaries but not across the boundaries.

CHAPTER 3

THE PROPOSED IMAGE SEGMENTATION AND DENOISING METHOD

The purpose of the segmentation and denoising problem is to find a piecewise smooth representation of a noisy image. The Mumford-Shah variational model is highly used in various image segmentation applications. It includes all the requirements for proper segmentation, i.e., the boundary detection of piecewise smooth regions and denoising. In this chapter, the Mumford-Shah modeling will be explained in detail. Then, the approximate Mumford-Shah gradient flow and the Chan-Vese active contour methods used for segmentation are elucidated. After the profound explanation, the comparisons of these methods are made in the sense of their computation times, and the hierarchical four-phase segmentation approaches based on these methods are given. Finally, the usage of the noise compensating diffusion filters in the images are demystified, and an image segmentation and denoising method is proposed. Then, the method is compared with the normalized cuts method.

3.1 The Mumford-Shah Model

The Mumford-Shah model relates the segmentation and denoising problem to a variational problem of minimizing an energy functional, namely the Mumford-Shah functional. In this section, the direct solution of minimization of the energy functional which is obtained in [10] is discussed explicitly.

Firstly, the image is interpreted as a function $g(x, y)$ defined in the image domain that is denoted by Ω . The domain Ω can be composed of various open subsets, i.e.,

$$\Omega = \Omega_1 \cup \Omega_2 \cup \dots \cup \Omega_n \quad (3.1)$$

where Ω_i is an open subset of Ω . A simple image whose image domain is formed by the two open subsets is shown in Figure 3.1.

The segmentation of image g is achieved when

- the image function $g(x, y)$ is homogeneous and/or varies smoothly within each Ω_i ,
- the image $g(x, y)$ is discontinuous across most of the boundary between different Ω_i s.

The segmentation problem can be restated as the approximation of the image function $g(x, y)$ by a piece-wise smooth function $f(x, y)$. This function can be considered as the combination of subfunctions $f_i(x, y)$ which are differentiable in Ω_i .

Using the Mumford-Shah functional the requirements of the segmentation problem is put into formulation. The energy functional E is constructed as,

$$E(f, \vec{C}) = \lambda \iint_{\Omega} (f - g)^2 dx dy + \eta \iint_{\Omega - \vec{C}} |\nabla f|^2 dx dy + \mu \oint_{\vec{C}} ds \quad (3.2)$$

where λ, η, μ are positive real constants and f is a differentiable function in the open subsets of Ω , which can be discontinuous across the boundary curves \vec{C} . The last term of the functional above stands for the total length of the arcs making up \vec{C} .

In the functional,

- the first term asks that f approximates g ,
- the second term asks that f does not vary very much in each Ω_i ,
- the third term asks that the arcs making up \vec{C} satisfying the previous statements are as short as possible.

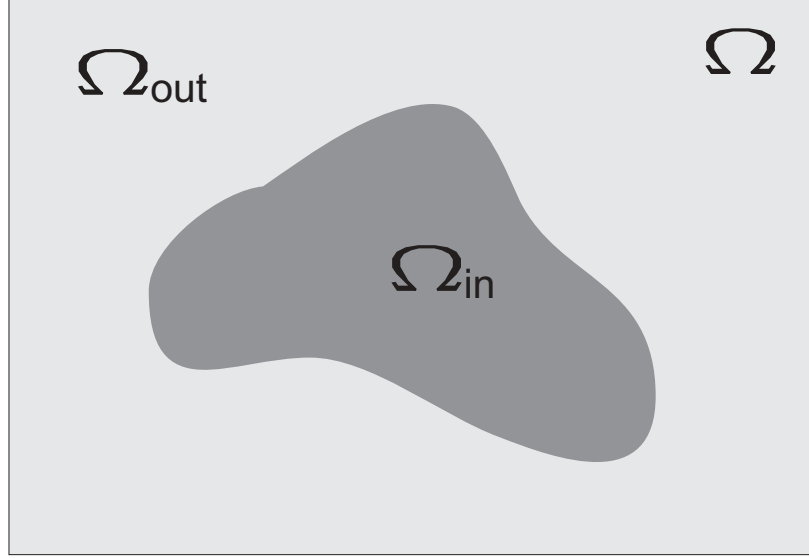


Figure 3.1: A simple image composed of two various open subsets.

As a result, the smaller the energy functional E is, the better the combination of f and \vec{C} segments the image g . The fundamental problem is to find the variables f and \vec{C} minimizing the functional E simultaneously, which is not an easy task due to the complex structure of the energy functional. Thus, two step minimization scheme is applied. In the first step, \vec{C} is fixed and E is minimized with respect to f . Similarly, f is fixed and E is minimized with respect to \vec{C} in the second one. The constants used for scaling purposes, they are fixed during the minimization steps.

The standard calculus of variations method is applied for the first step. δf is the same type of function as f and represents a small change in f . The difference equation relating the small variations in f is written as

$$\begin{aligned}
 E(f + t\delta f, \vec{C}) - E(f, \vec{C}) &= t[2\lambda \iint_{\Omega} \delta f(f - g)dx dy \\
 &\quad + 2\eta \iint_{\Omega - \vec{C}} (\nabla(\delta f) \cdot \nabla f)dx dy] \\
 &\quad + t^2[\lambda \iint_{\Omega} (\delta f)^2 dx dy + \eta \iint_{\Omega - \vec{C}} |\nabla(\delta f)|^2 dx dy].
 \end{aligned} \tag{3.3}$$

Then,

$$\begin{aligned}\frac{\delta E}{\delta f}(f, \vec{C}) &= \lim_{t \rightarrow 0} \frac{E(f + t\delta f, \vec{C}) - E(f, \vec{C})}{t} \\ &= 2[\lambda \iint_{\Omega} \delta f(f - g) dx dy + \eta \iint_{\Omega - \vec{C}} (\nabla(\delta f) \cdot \nabla f) dx dy]\end{aligned}\quad (3.4)$$

is obtained. Integrating by parts and using the Green's theorem, (3.4) is modified

$$\begin{aligned}\frac{1}{2} \frac{\delta E}{\delta f}(f, \vec{C}) &= \lambda \iint_{\Omega - \vec{C}} \delta f(f - g) dx dy + \eta \iint_{\Omega - \vec{C}} \delta f \nabla^2 f dx dy + \eta \oint_{\vec{C}} \delta f \frac{\partial f}{\partial \vec{N}} ds \\ &= \iint_{\Omega - \vec{C}} \delta f(\lambda(f - g) - \eta \nabla^2 f) dx dy + \eta \oint_{\vec{C}} \delta f \frac{\partial f}{\partial \vec{N}} ds.\end{aligned}\quad (3.5)$$

where \vec{N} is the outward normal vector of curve \vec{C} .

Since δf is nonzero in $\Omega - \vec{C}$ and zero elsewhere, f satisfies the damped Poisson equation with Neumann boundary condition as shown below.

$$\nabla^2 f = \frac{\lambda}{\eta}(f - g) \quad \text{in } \Omega - \vec{C} \quad (3.6)$$

$$\frac{\partial f}{\partial \vec{N}} = 0 \quad \text{on } \vec{C} \quad (3.7)$$

For the simple image which is composed of two homogeneous image regions and the curve separating these homogeneous regions as shown in Figure 3.1, the resulting equations can be written as

$$\nabla^2 f_{in} = \frac{\lambda_{in}}{\eta_{in}}(f_{in} - g) \quad \text{inside } \vec{C}, \quad \frac{\partial f_{in}}{\partial \vec{N}} = 0 \quad \text{on } \vec{C} \quad (3.8)$$

$$\nabla^2 f_{out} = \frac{\lambda_{out}}{\eta_{out}}(f_{out} - g) \quad \text{outside } \vec{C}, \quad \frac{\partial f_{out}}{\partial \vec{N}} = 0 \quad \text{on } \vec{C} \quad (3.9)$$

where f_{in} denotes the function f inside the curve \vec{C} and f_{out} denotes the function f outside the curve \vec{C} . λ_{in} , η_{in} and λ_{out} , η_{out} are the scaling parameters which enable the smoothing in different orders inside and outside \vec{C} , respectively. Normally, these constants are chosen as $\lambda_{in} = \lambda_{out}$ and $\eta_{in} = \eta_{out}$.

For the second minimization step, f is fixed and the curve \vec{C} separating the smooth regions is tried to be determined. Considering the simple image case as

shown in Figure 3.1, (3.2) can be reconstructed as

$$E(\vec{C}) = \lambda_{in} \iint_{in \vec{C}} (f_{in} - g)^2 dx dy + \lambda_{out} \iint_{out \vec{C}} (f_{out} - g)^2 dx dy \quad (3.10)$$

$$+ \eta_{in} \iint_{in \vec{C}} |\nabla f_{in}^2| dx dy + \eta_{out} \iint_{out \vec{C}} |\nabla f_{out}^2| dx dy + \mu \oint_{\vec{C}} ds.$$

A curve evolution process can be derived that minimizes (3.10) according to the variation of \vec{C} with respect to time t , i.e., $\frac{\partial \vec{C}}{\partial t}$. Since (3.10) is composed of four region integrals and the arc-length calculating the line integral, the curve evolution is determined by the combination of results of the gradient flow methods which are explained in Section 2.2. It is noted that inward normal vectors for the conjugate integral regions, i.e., inside and outside of curve \vec{C} , are collinear but in the opposite direction. When the direction of the normal vectors are taken into account, the curve evolution equation, namely the Mumford-Shah gradient flow, is attained as

$$\frac{\partial \vec{C}}{\partial t} = (\lambda_{in}(f_{in} - g)^2 - \lambda_{out}(f_{out} - g)^2) \vec{N}$$

$$+ (\eta_{in} |\nabla f_{in}^2| - \eta_{out} |\nabla f_{out}^2|) \vec{N} + \mu \kappa \vec{N}$$
(3.11)

where \vec{N} is the inward normal vector corresponding to the region inside the curve \vec{C} .

A proper segmentation algorithm based on the smoothing and curve evolution results works in an iterative manner. During an iteration step, the resulting regional smooth approximations of image function g , i.e., f_{in} and f_{out} , are the inputs for determining the evolving curve \vec{C} and vice versa. The results of direct solution to the Mumford-Shah functional on real and synthetic images can be found in [22].

3.2 Fundamentals of the Proposed Method

The direct solution of Mumford-Shah model for segmentation requires PDE solutions for the noise removal process as indicated in the previous section. However, denoising via PDEs has some disadvantages [8] such as low denoising capability and high computation time.

Detection of the boundaries between the homogeneous regions addresses the placement of these regions in the image domain. Therefore, once the closed curves separating the regions have been found, the regions inside and outside the curves can be denoised with a proper type of filter. This filter can be one of the diffusion filters because of their high denoising capability.

As a result, the curve evolution prior to the denoising method is chosen as the effective segmentation and denoising method due to its low computation time and high denoising capability. According to the experimental results, it is found that the curve evolution methods, namely the approximate Mumford-Shah gradient flow method and the Chan-Vese active contour method, satisfy the needs for proper segmentation.

In the following sections, the Chan-Vese active contour method and the implementation of the approximate Mumford-Shah gradient flow method via level set methods are explained. A hierarchical segmentation approach which is the combination of the investigated curve evolution methods is proposed. Finally, the effects of the nonlinear isotropic diffusion filters and the anisotropic diffusion on an image as the prefiltering and denoising after segmentation schemes are discussed.

The simulations on these topics are performed on a PC with AMD 2500+ CPU and 512 MB of RAM by running codes in the MATLAB environment.

3.2.1 Active Contours without Edges

An approximated form of the Mumford-Shah model in order to detect the edges in an image is introduced by Chan-Vese [5]. A simplification on the previously explained piecewise smooth function f is made by setting average intensity values in the image domains, i.e., Ω_i . In their framework, it is aimed to find the boundaries of the objects via an evolving implicit surface that is the result of energy minimization of their model.

It is explicit to develop the model for a simple image g which is composed of two piecewise smooth regions g_{in} , g_{out} and \vec{C}_o , the curve separating the smooth regions, i.e.,

$$g = g_{in} \cup g_{out} \cup \vec{C}_o. \quad (3.12)$$

The simple segmenting functional is

$$F(\vec{C}) = F_1(\vec{C}) + F_2(\vec{C}) = \lambda_{in} \iint_{in \vec{C}} (g - c_{in})^2 dx dy + \lambda_{out} \iint_{out \vec{C}} (g - c_{out})^2 dx dy \quad (3.13)$$

where \vec{C} is a variable curve that tracks \vec{C}_o ; c_{in} and c_{out} are the average values of the image inside and outside the curve \vec{C} ; and λ_{in} and λ_{out} are the positive real constants scaling the inside and outside energy terms $F_1(\vec{C})$ and $F_2(\vec{C})$, respectively. The minimizer of (3.13) is obviously

$$\inf_{\vec{C}} \{F(\vec{C})\} = \inf_{\vec{C}} \{F_1(\vec{C}) + F_2(\vec{C})\} \approx 0 \approx F_1(\vec{C}_o) + F_2(\vec{C}_o). \quad (3.14)$$

Inspecting (3.13), the conditions on $F_1(\vec{C})$ and $F_2(\vec{C})$ are found as

- $F_1(\vec{C}) > 0$ and $F_2(\vec{C}) \approx 0$ if \vec{C} is outside \vec{C}_o ,
- $F_1(\vec{C}) \approx 0$ and $F_2(\vec{C}) > 0$ if \vec{C} is inside \vec{C}_o ,
- $F_1(\vec{C}) > 0$ and $F_2(\vec{C}) > 0$ if \vec{C} is inside and outside \vec{C}_o ,
- $F_1(\vec{C}) \approx 0$ and $F_2(\vec{C}) \approx 0$ if \vec{C} is on \vec{C}_o .

The content of the energy functional in (3.13) does not satisfy the proper segmentation of an image. In order to make the energy functional suit with the requirements of segmentation, some regularization terms which are the length of \vec{C} and the area inside \vec{C} have been added. Since the values of c_{in} and c_{out} are varying depending on the position of evolving curve \vec{C} , they are included in the variable list of the functional F which becomes

$$F(\vec{C}, c_{in}, c_{out}) = \lambda_{in} \iint_{in \vec{C}} (g - c_{in})^2 dx dy + \lambda_{out} \iint_{out \vec{C}} (g - c_{out})^2 dx dy + \mu \oint_{\vec{C}} ds + \nu \iint_{in \vec{C}} dx dy \quad (3.15)$$

where λ_{in} , λ_{out} , μ and ν are the fixed scaling parameters. In the numerical calculations of this work, $\nu = 0$ and $\lambda_{in} = \lambda_{out} = \lambda$. The effects of the parameters λ_{in} , λ_{out} and μ are mentioned in the subsequent sections.

The main difference between (3.2) and (3.15) is that the variables c_{in} and c_{out} which represent the mean values of image parts inside and outside \vec{C} , respectively, are used in the latter model instead of the piecewise smooth representation of g inside and outside \vec{C} , i.e., f_{in} and f_{out} , respectively. This approximation results in a significant computational performance increase during the segmentation process, since the solutions of the PDEs (3.8) and (3.9) are not required for the curve evolution any more [8].

Another difference is the last term in (3.15) which is the requirement for the minimal area in \vec{C} . As indicated in [5], this term generally is not required in the segmentation process.

The minimization of the Chan-Vese energy functional can be achieved using the level set methods. According to these methods, the interfacing curve \vec{C} among the piecewise smooth regions is replaced by the Lipschitz continuous level set function $\phi(x, y)$ such that

$$\vec{C} = \{(x, y) \in \Omega : \phi(x, y) = 0\}. \quad (3.16)$$

Under this modification, (3.15) changes to

$$\begin{aligned} F(\phi, c_{in}, c_{out}) = & \lambda_{in} \iint_{\phi > 0} (g - c_{in})^2 dx dy + \lambda_{out} \iint_{\phi < 0} (g - c_{out})^2 dx dy \\ & + \mu \oint_{\phi=0} ds + \nu \iint_{\phi > 0} dx dy. \end{aligned} \quad (3.17)$$

In order to define the double integrating terms in one common boundary term, a Heaviside function $H(\phi)$ and its one-dimensional Dirac measure δ_0 concentrated at zero are defined by

$$H(\phi) = \begin{cases} 1, & \text{if } \phi \geq 0, \\ 0, & \text{if } \phi < 0 \end{cases} \quad (3.18)$$

$$\delta(\phi) = \frac{d}{d\phi} H(\phi). \quad (3.19)$$

The terms corresponding to length and area in (3.15) are expressed in [6] in terms of $H(\phi)$ as

$$\text{Length}(\Gamma) = \iint_{\Omega} |\nabla H(\phi)| dx dy, \quad (3.20)$$

$$\text{Area}(\Gamma) = \iint_{\Omega} H(\phi) dx dy. \quad (3.21)$$

Then, the terms of regularized energy functional F in (3.17) are expressed as

$$\iint_{\phi>0} (g - c_{in})^2 dx dy = \iint_{\Omega} (g - c_{in})^2 H(\phi(x, y)) dx dy \quad (3.22)$$

$$\iint_{\phi<0} (g - c_{out})^2 dx dy = \iint_{\Omega} (g - c_{out})^2 [1 - H(\phi(x, y))] dx dy \quad (3.23)$$

$$\begin{aligned} \oint_{\phi=0} ds &= \iint_{\Omega} |\nabla H(\phi(x, y))| dx dy \\ &= \iint_{\Omega} \delta_0(\phi(x, y)) |\nabla \phi(x, y)| dx dy \end{aligned} \quad (3.24)$$

$$\iint_{\phi>0} dx dy = \iint_{\Omega} H(\phi(x, y)) dx dy. \quad (3.25)$$

Additionally, the mean values of the separated regions for the fixed ϕ are

$$c_{in}(\phi) = \frac{\iint_{\Omega} g(x, y) H(\phi(x, y)) dx dy}{\iint_{\Omega} H(\phi(x, y)) dx dy} \quad (3.26)$$

$$c_{out}(\phi) = \frac{\iint_{\Omega} g(x, y) (1 - H(\phi(x, y))) dx dy}{\iint_{\Omega} (1 - H(\phi(x, y))) dx dy}. \quad (3.27)$$

After the updates mentioned above, the energy functional takes its final form as

$$\begin{aligned} F(\phi, c_{in}, c_{out}) &= \lambda_{in} \iint_{\Omega} (g - c_{in})^2 H(\phi(x, y)) dx dy \\ &+ \lambda_{out} \iint_{\Omega} (g - c_{out})^2 [1 - H(\phi(x, y))] dx dy \\ &+ \mu \iint_{\Omega} \delta_0(\phi(x, y)) |\nabla \phi(x, y)| dx dy + \nu \iint_{\Omega} H(\phi(x, y)) dx dy \end{aligned} \quad (3.28)$$

Parameterizing ϕ with artificial time $t \geq 0$ and minimizing the variational energy function with respect to ϕ using calculus of variations, the associated Euler-Lagrange equation (see Appendix A) is obtained as

$$\frac{\partial \phi}{\partial t} = \delta_0(\phi) \left[\mu \left(\nabla \cdot \frac{\nabla \phi}{|\nabla \phi|} \right) - \nu - \lambda_{in} (g - c_{in})^2 + \lambda_{out} (g - c_{out})^2 \right] = 0 \text{ in } (0, \infty) \times \Omega. \quad (3.29)$$

The initial and boundary conditions are

$$\phi(x, y, 0) = \phi_0(x, y) \text{ in } \Omega \text{ and } \frac{\delta_0(\phi)}{|\nabla \phi|} \frac{\partial \phi}{\partial \vec{N}} = 0 \text{ on } \partial \Omega \quad (3.30)$$

where \vec{N} is the exterior normal to the boundary $\partial \Omega$.

Since ϕ is a surface in three dimensions, (3.29) shows the change of the surface with respect to time t , and it states that the change takes place only at the locations where $\phi(x, y, t) = 0$, i.e., the contour on the image domain. This result is obtained from the existing delta Dirac function. However, updating only at these points is not proper from the practical point of view. The numerical explanations will make this indication more explicit.

As a result of the Chan-Vese active contour method, an image is segmented into two parts with respect to the two mean values. Each part can be composed of homogeneous regions whose mean values are close to that of the image part they are belonging to. These regions are separated by the zero level of the level set function ϕ as shown in Figure 3.2.

In order to implement the Chan-Vese active contour model, some numerical approximations have to be made. The finite difference method is used in order to discretize (3.29). The useful notations for the discretization are given as follows: h is the space step to define the grid points, i.e., $(x_i, y_j) = (ih, jh)$ where (i, j) forms the pixel index on an image. Taking Δt as the time step, the time approximation of $\phi(x_i, y_j, t)$ is denoted by $\phi_{i,j}^n = \phi(n\Delta t, x_i, y_j)$ with $n \geq 0$ and ϕ^0 is the initial ϕ . The finite differences are

$$\begin{aligned}
\Delta_-^x \phi_{i,j} &= \phi_{i,j} - \phi_{i-1,j} \\
\Delta_-^y \phi_{i,j} &= \phi_{i,j} - \phi_{i,j-1} \\
\Delta_+^x \phi_{i,j} &= \phi_{i+1,j} - \phi_{i,j} \\
\Delta_+^y \phi_{i,j} &= \phi_{i,j+1} - \phi_{i,j}.
\end{aligned} \tag{3.31}$$

The former two differences are known as the backward differences, and the latter two differences are the forward differences. Finally, embedding the discretization of the divergence operator from [16], and computing the average values $c_1(\phi^n)$ and $c_2(\phi^n)$ according to (3.26), the numerical model for (3.29) is obtained as

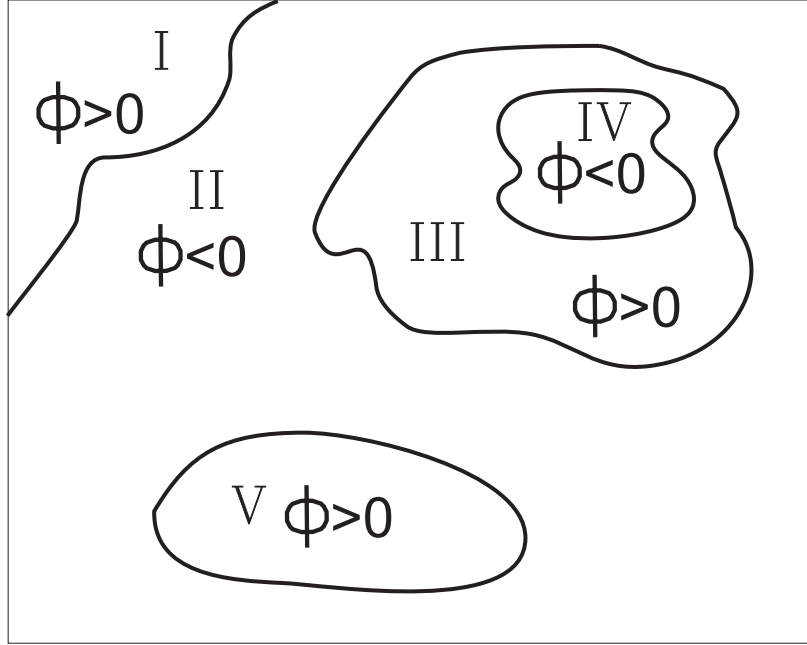


Figure 3.2: The separated homogeneous regions and the corresponding ϕ values in these regions.

$$\begin{aligned}
\frac{\phi_{i,j}^{n+1} - \phi_{i,j}^n}{\Delta t} = \delta_h(\phi_{i,j}^n) & \left[\frac{\mu}{h^2} \Delta_x^- \cdot \left(\frac{\Delta_x^+ \phi_{i,j}^{n+1}}{\sqrt{(\Delta_x^+ \phi_{i,j}^n)^2 / (h^2) + (\phi_{i,j+1}^n - \phi_{i,j-1}^n)^2 / (2h)^2}} \right) \right. \\
& + \frac{\mu}{h^2} \Delta_y^- \cdot \left(\frac{\Delta_y^+ \phi_{i,j}^{n+1}}{\sqrt{(\Delta_y^+ \phi_{i,j}^n)^2 / (h^2) + (\phi_{i+1,j}^n - \phi_{i-1,j}^n)^2 / (2h)^2}} \right) \\
& \left. - \nu - \lambda_1 (g_{i,j} - c_1(\phi^n))^2 + \lambda_2 (g_{i,j} - c_2(\phi^n))^2 \right]. \quad (3.32)
\end{aligned}$$

In the experiments, the parameters h and Δt are chosen as $h = 1$ and $\Delta t = 0.1$.

Consequently, the order of the steps of the Chan-Vese active contour computation algorithm is formed as

- initialize the level set function ϕ , i.e., ϕ^0 ,
- calculate the mean values inside and outside the zero level of ϕ , i.e., $c_1(\phi^n)$ and $c_2(\phi^n)$, respectively,

- find the Heaviside and delta Dirac functions, i.e., $H_h(\phi^n)$ and $\delta_h(\phi^n)$, respectively,
- calculate the energy change which is the right-hand side of (3.32) and obtain ϕ^{n+1} ,
- enter the loop from the second step until the solution is stable. For the next iteration, ϕ^{n+1} is the initial condition, i.e., $\phi^n \Leftarrow \phi^{n+1}$.

Figure 3.3 shows the evolution of ϕ and its corresponding zero level curve with respect to time. The identification of most of the edge points occurs at the starting iterations of evolution; because at these iterations the mean values c_{in} and c_{out} are far from their final values, and the value of the right hand-side of (3.29) for each pixel is high enough to change the state of ϕ on the relevant grid points, i.e., $\phi^n(x_i, y_j) < 0$ and $\phi^{n+1}(x_i, y_j) > 0$ or vice versa. As the iteration count increases, the number of state changing pixels decreases.

Secondly, approximations of the Heaviside function H and so does the delta Dirac function δ_0 are proposed for the numerical calculation of update term for ϕ according to time steps in (3.29). Possible approximations of H are given in [30] as

$$H_{1,\epsilon}(\phi) = \begin{cases} 1, & \text{if } \phi > \epsilon \\ 0, & \text{if } \phi < -\epsilon \\ \frac{1}{2} \left[1 + \frac{\phi}{\epsilon} + \frac{1}{\pi} \sin\left(\frac{\pi\phi}{\epsilon}\right) \right], & \text{if } |\phi| \leq \epsilon \end{cases} \quad (3.33)$$

and in [5] as

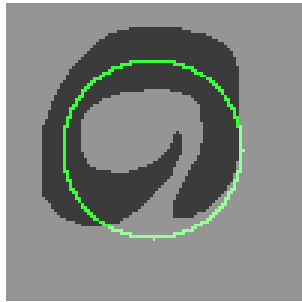
$$H_{2,\epsilon}(\phi) = \frac{1}{2} \left(1 + \frac{2}{\pi} \arctan\left(\frac{\phi}{\epsilon}\right) \right). \quad (3.34)$$

where ϵ denotes the infinitesimal change around zero.

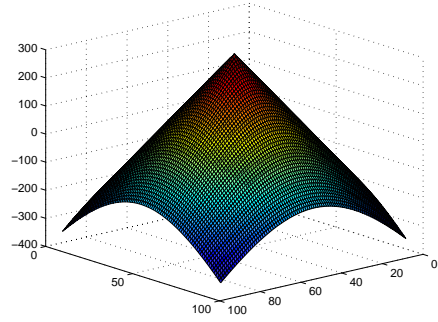
Taking the derivatives of (3.33) and (3.34), the relevant delta Dirac functions are found as

$$\delta_{1,\epsilon}(\phi) = \begin{cases} 0, & \text{if } |\phi| > \epsilon \\ \frac{1}{2\epsilon} \left[1 + \cos\left(\frac{\pi\phi}{\epsilon}\right) \right], & \text{if } |\phi| \leq \epsilon \end{cases} \quad (3.35)$$

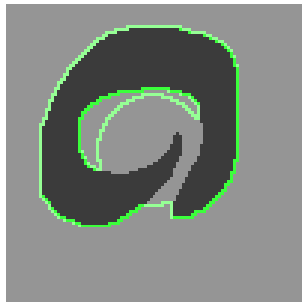
$$\delta_{2,\epsilon}(\phi) = \frac{1}{\pi} \frac{\epsilon}{\epsilon^2 + \phi^2} \quad (3.36)$$



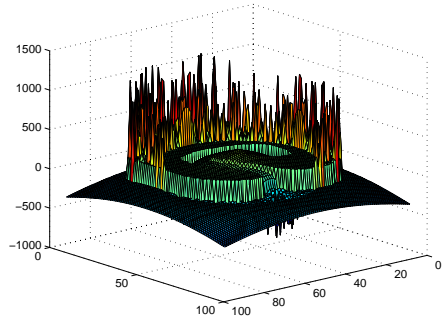
(a)



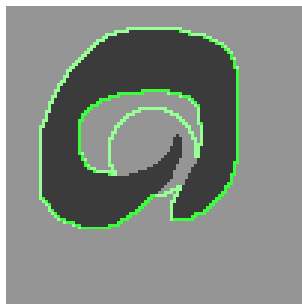
(b)



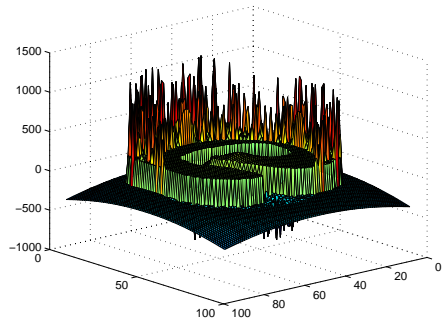
(c)



(d)

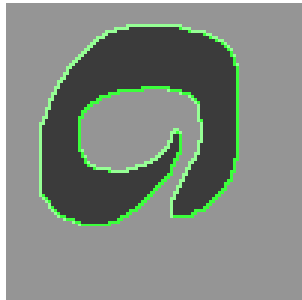


(e)

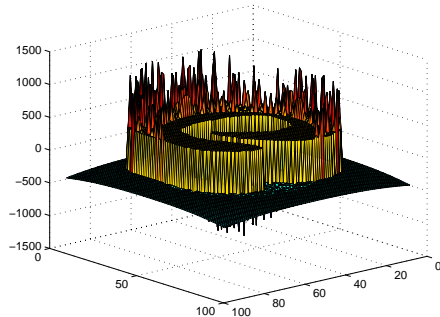


(f)

Figure 3.3: The evolution of the curve on the synthetic image (left column) and the corresponding evolution of the level set function for the Chan-Vese active contour method (right column).



(g)

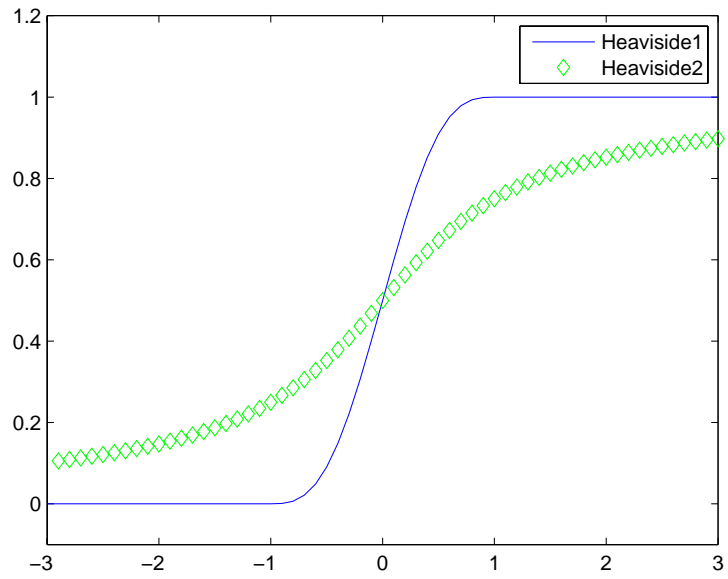


(h)

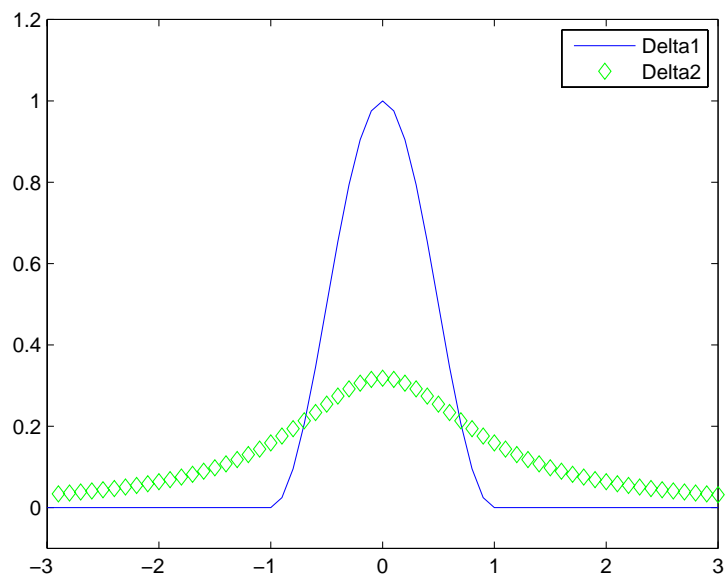
Figure 3.3: continued

which are also shown in Figure 3.4. As $\epsilon \rightarrow 0$, the approximate Heaviside functions $H_{1,\epsilon}$ and $H_{2,\epsilon}$ converge to the ideal case in (3.18), so does the delta Dirac functions $\delta_{1,\epsilon}$ and $\delta_{2,\epsilon}$. $\delta_{1,\epsilon}$ is nonzero in the interval $[-\epsilon, \epsilon]$, whereas $\delta_{2,\epsilon}$ is nonzero in the image domain. Consequently, using $H_{1,\epsilon}$ and $\delta_{1,\epsilon}$ for updating of ϕ takes place on a few level curves above and below the zero level. The zero level of ϕ evolves as if it were a snake and can not detect the interior contours. However, change in ϕ takes place at all levels when (3.29) is implemented via $H_{2,\epsilon}$ and $\delta_{2,\epsilon}$. This property enables the zero level of ϕ appear not only surrounding the exterior boundary of a smooth region but also the interior boundary. This statement will be made clear later. In this work, $H_{2,\epsilon}$ and $\delta_{2,\epsilon}$ are taken as the numerical approximations to the Heaviside function H and the delta Dirac function around zero δ_0 in (3.29), and ϵ is set to 1.

The selection of the initial ϕ can be achieved in various ways. In Figure 3.5, in order to investigate the effect of the initial ϕ selection on the performance of the mentioned method, five different initial conditions on ϕ are given. For the first run, the initial ϕ is chosen such that it does not result in a contour curve on the image plane. For the remaining four runs, the initial conditions on ϕ are given such that its zero level is outside the object boundary, crossing



(a)

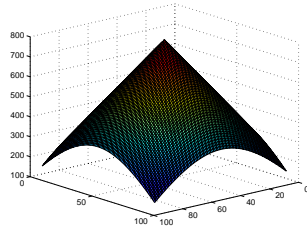


(b)

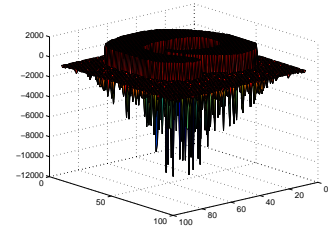
Figure 3.4: Two different approximations of (a) the Heaviside function and (b) the delta Dirac function.



(a)



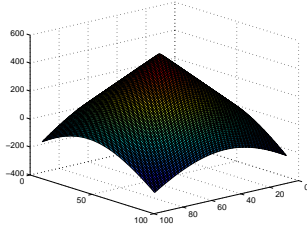
(b)



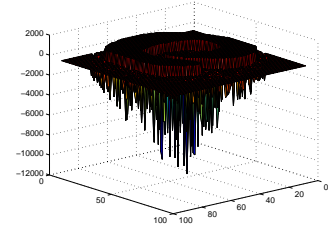
(c)



(d)



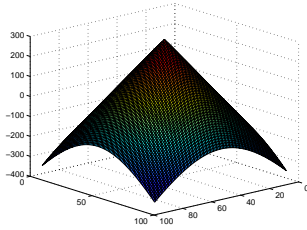
(e)



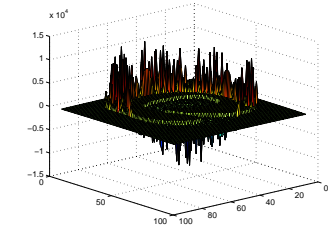
(f)



(g)



(h)

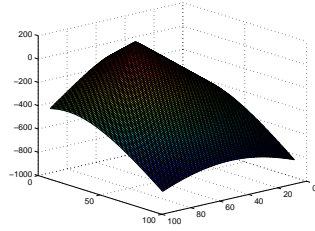


(i)

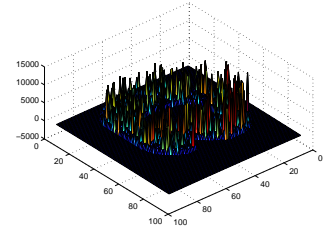
Figure 3.5: Segmentation results of the Chan-Vese active contour method with respect to different initial conditions. The first and the second columns show the initial curves on the 100 x 100 synthetic image and the corresponding level set function ϕ_0 . The third column is the final level set function ϕ and (p) is the segmentation result of the different initial conditions. $\mu = 0.01 \times 255^2$, $\lambda = 10$.



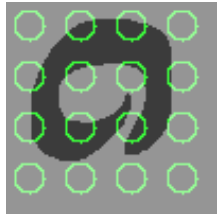
(j)



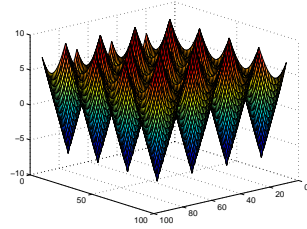
(k)



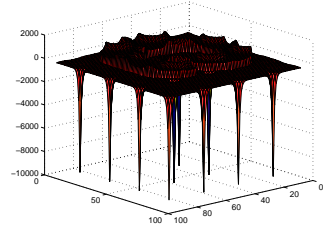
(l)



(m)



(n)



(o)



(p)

Figure 3.5: continued

the object boundary, inside the object boundary and composed of more than one curve on the image plane, respectively. Independent of the selection of initial ϕ , the final zero level of ϕ converges to the object boundary. However, the time it takes for the algorithm to converge to the object boundary is highly affected by the selection of initial ϕ . The CPU temporal performances according to the mentioned five different initial conditions are 907.3 s, 98.9 s, 25.5 s, 136.2 s, 0.2 s, respectively. Among the first four initial conditions, the one with zero level crosses the boundary of the object gives the best time of convergence to the object boundary. Unfortunately, it is not always possible to know the placement of the object boundary in different applications. Thus, the selection of the initial ϕ whose zero level is composed of closed curves regularly distributed on the whole image increases the chance of the zero level crossing the object boundaries at two or more points. This selection is resulted in a much better CPU performance.

Another advantage of the Chan-Vese active contour method over the classical snake methods can be seen for the case when there are more than one object boundary inside one another, as in Figure 3.6. This is the direct result of using the approximated delta Dirac function explained previously. Using this function, the effect of minimizer in (3.29) can be seen at all levels of the function ϕ . As the zero level of ϕ detects the outer boundary of the object, it does not stop changing due to the mean value changes in the interior of the object boundary. The zero level of ϕ keeps on changing until it also detects the interior boundary.

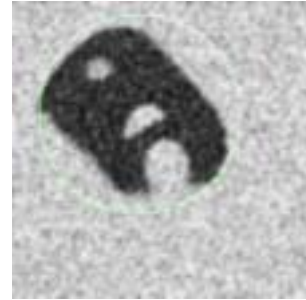
According to [5] and [8], the choice of the parameters μ , λ_{in} and λ_{out} has an effect on the speed of convergence of the numerical results and the sizes of the detected objects in the image. When the value of μ decreases, the algorithm speeds down and the small objects in the image are detected. This is due to the fact that for small μ the terms with λ_{in} and λ_{out} are more effective in (3.29). However, in noisy images spikes can be seen in the smooth regions. In order not to detect these spikes, μ has to be large enough. The relation between μ and the variance of the noisy image, σ^2 , is indicated in [8] as

$$\mu = \beta\sigma^2 \tag{3.37}$$

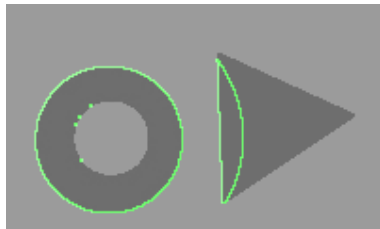
where β is a constant between 0 and 1.5. In this work, for the segmentation of



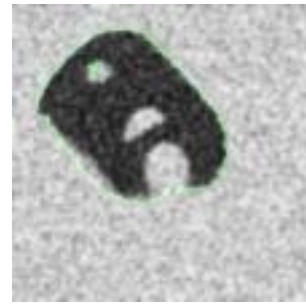
(a)



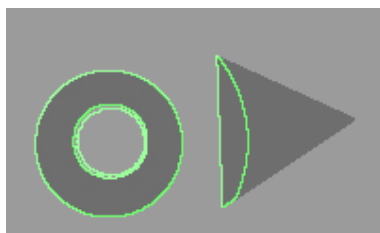
(b)



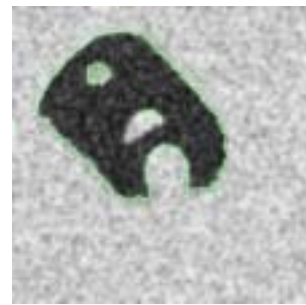
(c)



(d)

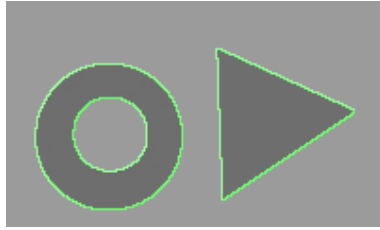


(e)

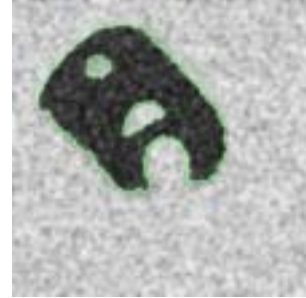


(f)

Figure 3.6: The detection of the interior boundary of the objects when the initial zero level of ϕ is outside the outer boundary.



(g)



(h)

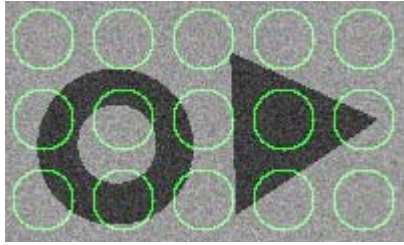
Figure 3.6: continued

noisy images, β is taken as 0.5 or 2. Additionally, λ_{in} and λ_{out} are effective in the subregions Ω_{in} and Ω_{out} , respectively, considering the simple image case in Figure 3.1. Thus, the larger the parameters λ_{in} and λ_{out} , the most probable that the variations in the subregions appear in the zero level of ϕ . After mentioning all of these details, some real image applications are given in Figure 3.7.

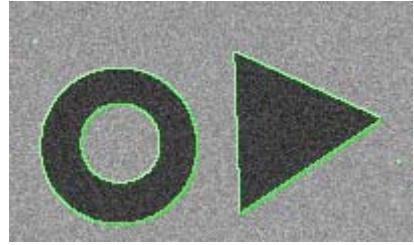
In some images, smooth regions having comparable mean values may be located one inside the other. In these cases, the evolving zero level of ϕ is at the outermost boundary. In order to handle this problem, another level set function have to be implemented. This issue will be clarified in Section 3.2.3.

3.2.2 Approximated Mumford-Shah Flow

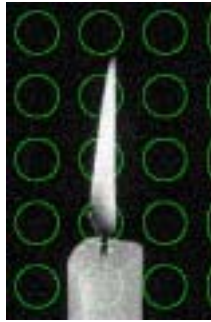
Another curve evolution method that can be used for the segmentation problems is the so called Mumford-Shah optical gradient flow method [10]. This method is found from the structure of the energy functional (3.2), where the smoothing function f is fixed. Since minimization of (3.10) includes minimizing the arc-lengths of closed curves and minimizing the region integrals which define



(a)



(b)



(c)



(d)

Figure 3.7: Segmentation of noisy images by the Chan-Vese active contours method. (a) 120 x 201 synthetic image with zero mean Gaussian white noise (SNR = 20dB). (b) Segmented synthetic image. $\mu = 2\sigma^2 = 3994$, $\lambda = 6$. Computation time is 83 s. (c) 300 x 196 burning candle image with zero mean Gaussian white noise (SNR = 10dB). (d) Segmented burning candle image. $\mu = 2\sigma^2 = 3798$, $\lambda = 6$. Computation time is 547.4 s.

the error and smoothness terms, the flows described in Section 2.2 suit with the needs. Since the terms related with the gradient flow for region integrals include the piecewise smooth function f , the mean values of the regions inside and outside \vec{C} can be used instead of f similar to the case in the previous curve evolution algorithm. This results in a useful computational simplification. Additionally, the outer normal vectors for the conjugate regions are in the opposite directions, meaning that the net movement at the boundary points can be found by subtracting the integrands of the region integrals. By combining these flows, the curve evolution equation can be found as

$$\frac{\partial \vec{C}}{\partial t} = \mu \kappa \vec{N} + [\lambda_{in}(g - c_{in})^2 - \lambda_{out}(g - c_{out})^2] \vec{N} \quad (3.38)$$

where μ , λ_{in} and λ_{out} are the coefficients mentioned previously.

For the implementation, the level set method is used in order to make robust boundary localization. Embedding curve evolution equation (3.38) to a Lipschitz continuous level set function ϕ is different than the previous one. The evolving zero level of ϕ , i.e., $\vec{C}(t)$, is defined as

$$\vec{C}(t) \in \mathbb{R}_2 : \phi(\vec{C}, t) = 0. \quad (3.39)$$

Differentiating (3.39) with respect to t

$$\nabla \phi(\vec{C}, t) \cdot \frac{\partial \vec{C}}{\partial t} + \frac{\partial \phi(\vec{C}, t)}{\partial t} = 0 \quad (3.40)$$

is obtained. For the zero level of ϕ , the inner normal vector can be found as

$$\frac{\nabla \phi}{|\nabla \phi|} = -\vec{N}. \quad (3.41)$$

Combination of equations (3.38), (3.40) and (3.41) resulted in the desired level set function ϕ , i.e.,

$$\frac{\partial \phi}{\partial t} = |\nabla \phi| \left[\mu \nabla \cdot \left(\frac{\nabla \phi}{|\nabla \phi|} \right) + [\lambda_{in}(g - c_{in})^2 - \lambda_{out}(g - c_{out})^2] \right] \quad (3.42)$$

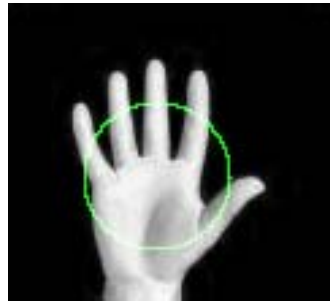
The only difference of this flow from the Chan-Vese active contour method is that it is more effective in the whole image because of the multiplier of the update term in (3.42), i.e., $|\nabla \phi|$.

The evolutions of ϕ and its corresponding zero level with respect to time are shown in Figure 3.8. All the numerical approximations and predefined algorithm steps are valid also for this method. The initialization of ϕ has no importance for this method, either. The five different initialization schemes for ϕ are given with the relevant results in Figure 3.9; the pertinent temporal CPU performances according to these initializations are the same, i.e., 1.6 s. Since the level set method is used for the implementation of this method, the interior boundaries of the objects are also detected, which is similar to the Chan-Vese active contour method.

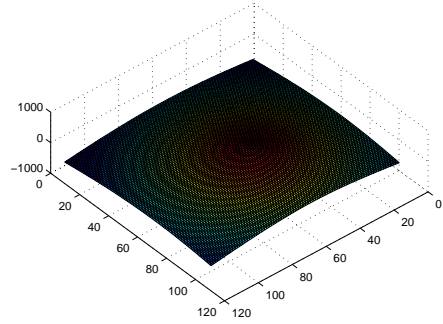
Resulting equations of the given two curve evolution schemes in Sections 3.2.1 and 3.2.2 are nearly the same. These ϕ updating equations are composed of multiplicative term and the difference term which is formed by adding the curvature term and the error terms in the mean square sense. In (3.42), the difference term between the two consecutive iterations of ϕ is multiplied with $|\phi|$. According to this statement, all the points on the surface ϕ are affected from the updates. Thus, its zero level moves fast and detects the boundary locations of piecewise smooth regions quickly. However, in (3.29), the points on the zero level and around the zero level of ϕ changes at most. As a result, its zero level evolves in a limited region in each iteration, which means a slower motion as compared to the Mumford-Shah gradient flow method. The segmentation durations for the two methods can be compared according to the results given in Figures 3.7 and 3.10.

3.2.3 Four-Phase Hierarchical Image Segmentation

Using one level set function, one can observe that the image is segmented into more than two piecewise smooth regions depending on the application. However, from the computational point of view such an image classified into two parts. This result can be obtained from (3.29), where the energy minimization is achieved via using two mean values. This type of segmentation is named as two-phase segmentation.



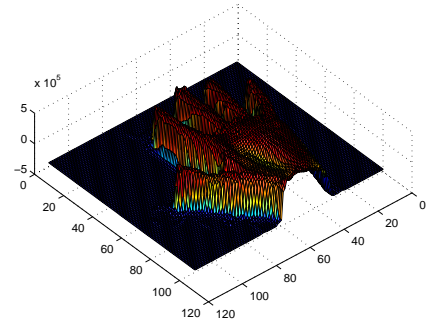
(a)



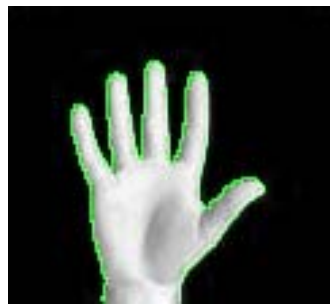
(b)



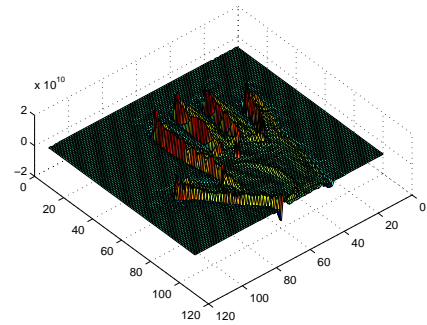
(c)



(d)



(e)

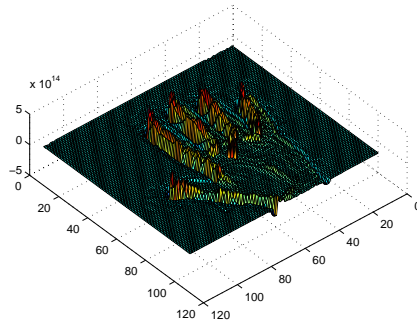


(f)

Figure 3.8: The evolution of the curve on the hand image (left column) and the corresponding evolution of the level set function for the approximate Mumford-Shah gradient flow method (right column).



(g)



(h)

Figure 3.8: continued

When two or more smooth regions whose average intensities are close to each other as compared to the rest of the image are adjoining or one inside the other, then these regions are regarded as one smooth region in two-phase segmentation. This is the case for regions *III* and *IV* in Figure 3.11. In order to segment these regions, more than one level set function has to be used. Therefore, the image is classified into four parts; this is called the four-phase segmentation. The relation between the number of phases, N_{phase} , and the number of required level set functions, N_ϕ , is given by

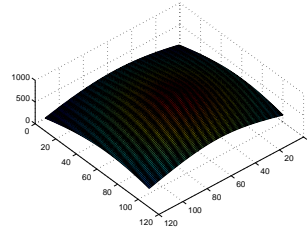
$$N_\phi = \log_2 N_{phase}. \quad (3.43)$$

The partitioning of the image domain with respect to two and three level set functions are given in Figure 3.12.

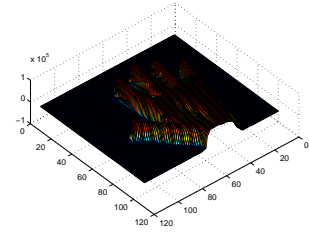
Observations show that the image segmentation with two level set functions satisfies the needs for most of the applications. In [24], the four-phase segmentation is accomplished via the energy functional



(a)



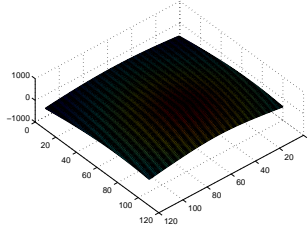
(b)



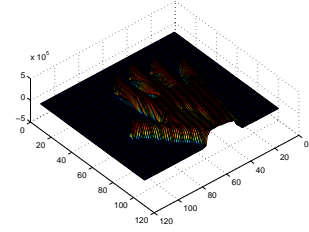
(c)



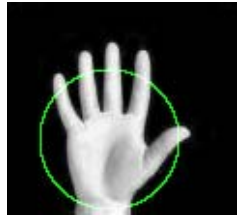
(d)



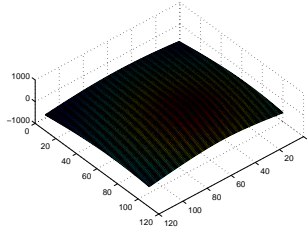
(e)



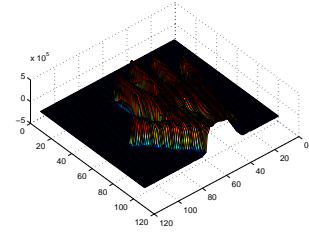
(f)



(g)

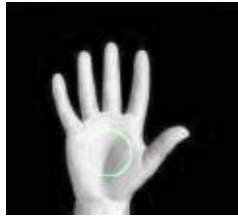


(h)

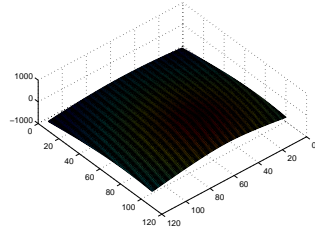


(i)

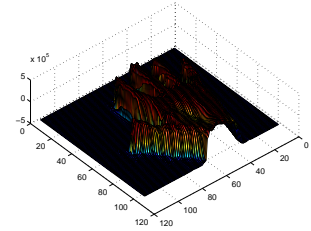
Figure 3.9: Segmentation results of the approximate Mumford-Shah gradient flow with respect to different initial conditions. The first and the second columns show the initial curves on the 100 x 100 hand image and the corresponding level set function ϕ_0 . The third column is the final level set function ϕ and (p) is the segmentation result of the different initial conditions. $\mu = 0.0001 \times 255^2$, $\lambda = 1$



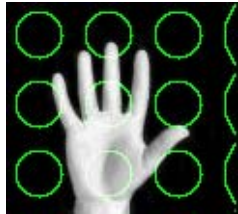
(j)



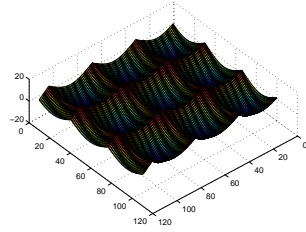
(k)



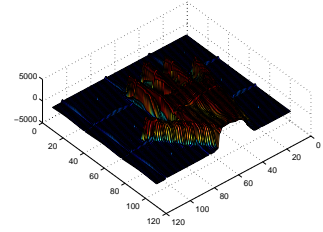
(l)



(m)



(n)

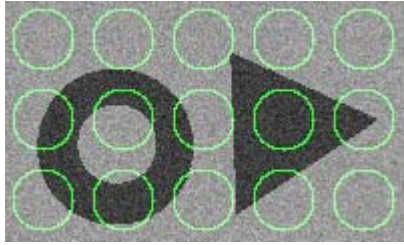


(o)

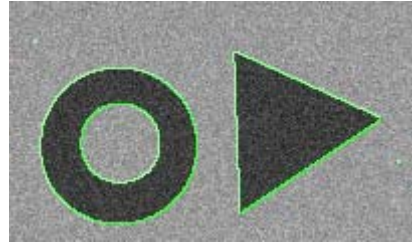


(p)

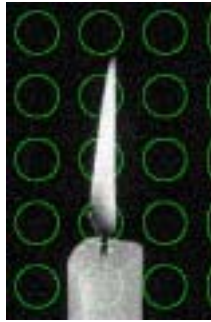
Figure 3.9: continued



(a)



(b)



(c)



(d)

Figure 3.10: Segmentation of noisy images by the approximate Mumford-Shah gradient flow method. $\mu = 0.0001 \times 255^2$, $\lambda = 1$. (a) 120×201 synthetic image with zero mean Gaussian white noise (SNR = 20dB). (b) Segmented synthetic image. Computation time is 3.2 s. (c) 300×196 burning candle image with zero mean Gaussian white noise (SNR = 10dB). (d) Segmented burning candle image. Computation time is 4.3 s.

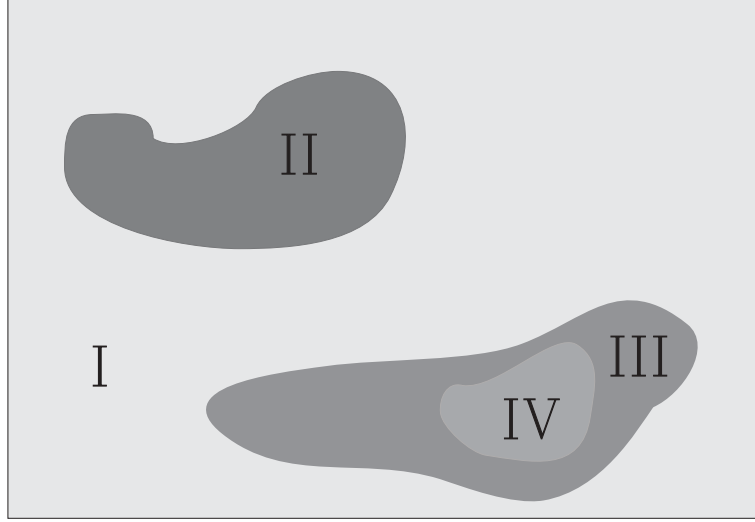
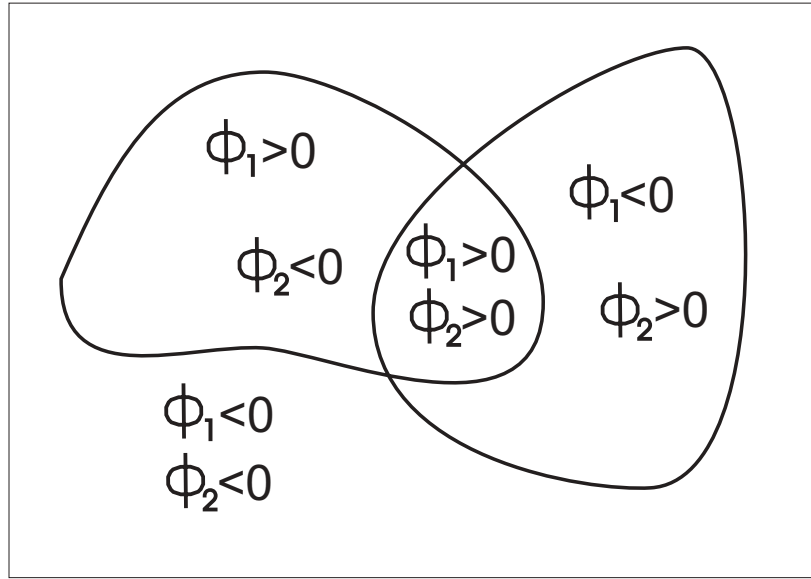


Figure 3.11: An image where two smooth regions with comparable mean values are one inside the other.

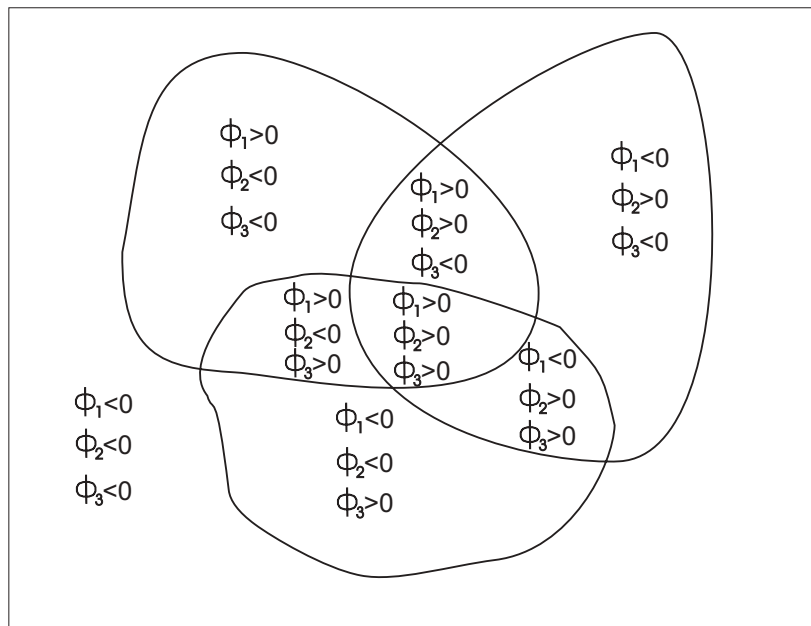
$$\begin{aligned}
F(\Phi, c) = & \lambda_{11} \iint_{\Omega} (g - c_{11})^2 H(\phi_1) H(\phi_2) dx dy \\
& + \lambda_{10} \iint_{\Omega} (g - c_{10})^2 H(\phi_1) [1 - H(\phi_2)] dx dy \\
& + \lambda_{01} \iint_{\Omega} (g - c_{01})^2 [1 - H(\phi_1)] H(\phi_2) dx dy \\
& + \lambda_{00} \iint_{\Omega} (g - c_{00})^2 [1 - H(\phi_1)] [1 - H(\phi_2)] dx dy \\
& + \mu_1 \iint_{\Omega} \delta_0(\phi_1) |\nabla \phi_1| dx dy + \mu_2 \iint_{\Omega} \delta_0(\phi_2) |\nabla \phi_2| dx dy \\
& + \nu_1 \iint_{\Omega} H(\phi_1) dx dy + \nu_2 \iint_{\Omega} H(\phi_2) dx dy \tag{3.44}
\end{aligned}$$

where $\Phi = (\phi_1, \phi_2)$ and $c = (c_{11}, c_{10}, c_{01}, c_{00})$ are the level set function and the constant vectors, respectively. Here

$$\begin{aligned}
c_{11} &= \text{mean}(g) \quad \text{when } \phi_1(x, y, t) > 0 \text{ and } \phi_2(x, y, t) > 0, \\
c_{10} &= \text{mean}(g) \quad \text{when } \phi_1(x, y, t) > 0 \text{ and } \phi_2(x, y, t) < 0, \\
c_{01} &= \text{mean}(g) \quad \text{when } \phi_1(x, y, t) < 0 \text{ and } \phi_2(x, y, t) > 0, \\
c_{00} &= \text{mean}(g) \quad \text{when } \phi_1(x, y, t) < 0 \text{ and } \phi_2(x, y, t) < 0.
\end{aligned}$$



(a)



(b)

Figure 3.12: (a) Two level set functions, ϕ_1 and ϕ_2 , partition the image domain into four regions. (b) Three level set functions, ϕ_1 , ϕ_2 and ϕ_3 , partition the image domain into eight regions.

Finally, the Euler-Lagrange equations for level set functions ϕ_1 and ϕ_2 can be found similar to the ones in Section 3.2.1 as

$$\begin{aligned} \frac{\partial \phi_1}{\partial t} = & \delta_0(\phi_1) \left[\mu_1 \left(\nabla \cdot \frac{\nabla \phi_1}{|\nabla \phi_1|} \right) - \nu_1 - [\lambda_{11}(g - c_{11})^2 - \lambda_{01}(g - c_{01})^2] H(\phi_2) \right. \\ & \left. + [\lambda_{10}(g - c_{10})^2 - \lambda_{00}(g - c_{00})^2] [1 - H(\phi_2)] \right] = 0, \end{aligned} \quad (3.45)$$

$$\begin{aligned} \frac{\partial \phi_2}{\partial t} = & \delta_0(\phi_2) \left[\mu_2 \left(\nabla \cdot \frac{\nabla \phi_2}{|\nabla \phi_2|} \right) - \nu_2 - [\lambda_{11}(g - c_{11})^2 - \lambda_{01}(g - c_{01})^2] H(\phi_1) \right. \\ & \left. + [\lambda_{10}(g - c_{10})^2 - \lambda_{00}(g - c_{00})^2] [1 - H(\phi_1)] \right] = 0. \end{aligned} \quad (3.46)$$

In this four-phase segmentation, the level set functions evolve simultaneously. The results of the simultaneous four-phase segmentation based on the Chan-Vese active contour method can be found in [24]. One handicap of the simultaneous four-phase image segmentation is that the decision of segmenting the image with one or two level sets has to be given at the start of processing after inspecting the image. If the starting decision is to use one level set function, and the result is not satisfactory, the implementation has to be restarted for the simultaneous level set evolution.

This obstacle can be handled via using decoupled level set functions. This algorithm is composed of two steps. In the first step of decoupled multiphase image segmentation, only one level set function evolves. If the segmentation does not satisfy the expectations according to the results of the first step, then the second level set function is activated. More steps can be added in order to segment more regions. The relevant Euler-Lagrange equations for the first and second steps of decoupled segmentation, i.e., the hierarchical four-phase segmentation based on the Chan-Vese active contour method, are

$$\frac{\partial \phi_1}{\partial t} = \delta_0(\phi_1) \left[\mu_1 \left(\nabla \cdot \frac{\nabla \phi_1}{|\nabla \phi_1|} \right) - \nu_1 - \lambda_1(g - c_1)^2 + \lambda_0(g - c_0)^2 \right] = 0 \quad (3.47)$$

$$\begin{aligned} \frac{\partial \phi_2}{\partial t} = & \delta_0(\phi_2) \left[\mu_2 \left(\nabla \cdot \frac{\nabla \phi_2}{|\nabla \phi_2|} \right) - \nu_2 - [\lambda_{11}(g - c_{11})^2 - \lambda_{01}(g - c_{01})^2] H(\phi_1) \right. \\ & \left. + [\lambda_{10}(g - c_{10})^2 - \lambda_{00}(g - c_{00})^2] [1 - H(\phi_1)] \right] = 0. \end{aligned} \quad (3.48)$$

Similarly, the PDEs for the hierarchical four-phase segmentation based on the approximate Mumford-Shah gradient flow method are given as

$$\frac{\partial \phi_1}{\partial t} = |\nabla \phi_1|(\phi_1) \left[\mu_1 \left(\nabla \cdot \frac{\nabla \phi_1}{|\nabla \phi_1|} \right) - \nu_1 - \lambda_1 (g - c_1)^2 + \lambda_0 (g - c_0)^2 \right] = 0, \quad (3.49)$$

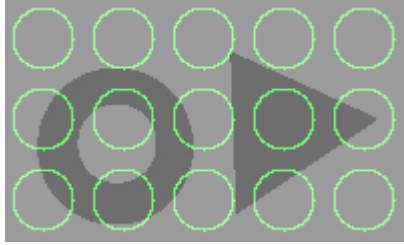
$$\begin{aligned} \frac{\partial \phi_2}{\partial t} = |\nabla \phi_2|(\phi_2) \left[\mu_2 \left(\nabla \cdot \frac{\nabla \phi_2}{|\nabla \phi_2|} \right) - \nu_2 - [\lambda_{11} (g - c_{11})^2 - \lambda_{01} (g - c_{01})^2] H(\phi_1) \right. \\ \left. + [\lambda_{10} (g - c_{10})^2 - \lambda_{00} (g - c_{00})^2] [1 - H(\phi_1)] \right] = 0. \end{aligned} \quad (3.50)$$

In the numerical calculations for the hierarchical four-phase segmentation in this work; $\nu_1 = \nu_2 = 0$, $\lambda_0 = \lambda_1$ and $\lambda_{00} = \lambda_{01} = \lambda_{10} = \lambda_{11} = \lambda_2$.

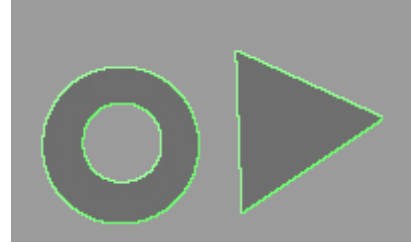
The results of the two hierarchical four-phase segmentation approaches on the synthetic images are given in Figures 3.13 and 3.14. In the first rows, it is seen that the segmentation of the smooth regions is achieved using one level set function. In the second rows, the insufficiency of using one level set function in order to segment the adjoining homogeneous regions with comparable mean values is shown. The last rows contain the segmentation results of using decoupled level set functions.

According to the observations, the hierarchical four-phase segmentation approach based on the approximate Mumford-Shah gradient flow method gives undesired results on some images due to the selected value of λ_2 . If it is set to a small value, the second level set function becomes positive at all points after a number of iterations, i.e., its zero level is not on the image plane. Conversely, if λ is large, not only the boundaries of the undetected regions in the first segmentation step but also the small variations in the previously segmented regions are detected. These unsatisfactory results are illustrated in Figures 3.15 and 3.16.

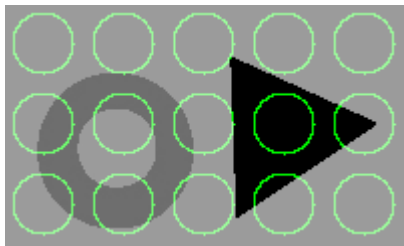
Comparing the two hierarchical four-phase segmentation approaches, the one based on the approximate Mumford-Shah gradient flow method converges faster to the boundary locations. However, in some cases it can not detect the boundaries properly. Hence, a fast hierarchical four-phase segmentation approach is formed via the combination of the two segmentation methods. At the first step, the approximate Mumford-Shah gradient flow method is used as the fast segmentation method. Second step is formed by the Chan-Vese active contour method.



(a)



(b)

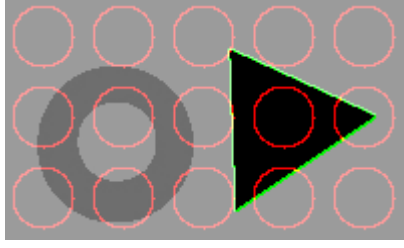


(c)

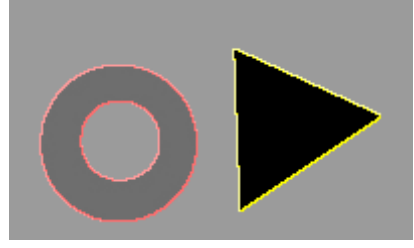


(d)

Figure 3.13: The hierarchical four-phase segmentation based on the Chan-Vese active contour method. Image size: 120×201 , $\mu_1 = \mu_2 = 0.0001 \times 255^2$, $\lambda_1 = \lambda_2 = 1$. (a) The synthetic image composed of three regions with two different mean values and the initial curves. (b) Segmentation result of (a). Computation time is 6.8 s. (c) The synthetic image composed of three regions with three different mean values and the initial curves belonging to the first step. (d) Segmentation result of the first step. Computation time is 14.4 s. (e) The initial curves belonging to the second step. (f) Segmentation result of the second step. Total computation time is 684.2 s.



(e)



(f)

Figure 3.13: continued

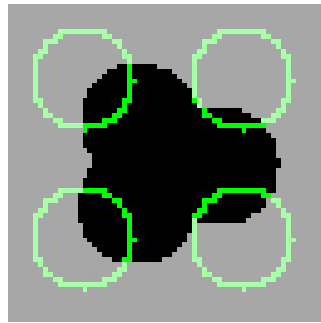
Thus, the Euler-Lagrange equations for the proposed hierarchical four-phase segmentation approach are given as

$$\frac{\partial \phi_1}{\partial t} = \delta_0(\phi_1) \left[\mu_1 \left(\nabla \cdot \frac{\nabla \phi_1}{|\nabla \phi_1|} \right) - \nu_1 - \lambda_1 (g - c_1)^2 + \lambda_0 (g - c_0)^2 \right] = 0 \quad (3.51)$$

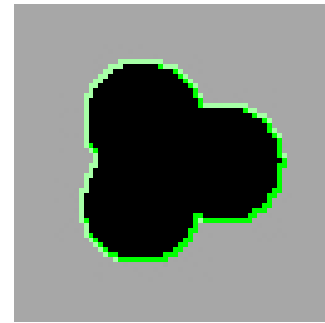
$$\begin{aligned} \frac{\partial \phi_2}{\partial t} = & |\nabla \phi_2| \left[\mu_2 \left(\nabla \cdot \frac{\nabla \phi_2}{|\nabla \phi_2|} \right) - \nu_2 - [\lambda_{11} (g - c_{11})^2 - \lambda_{01} (g - c_{01})^2] H(\phi_1) \right. \\ & \left. + [\lambda_{10} (g - c_{10})^2 - \lambda_{00} (g - c_{00})^2] [1 - H(\phi_1)] \right] = 0. \end{aligned} \quad (3.52)$$

The comparison of the proposed hierarchical four-phase segmentation approach and the one whose segmentation steps are based on the Chan-Vese active contour method are given in Figure 3.17. Additionally, segmentation of the well-known house image by the proposed method results in suitable segments, (see Figure 3.18).

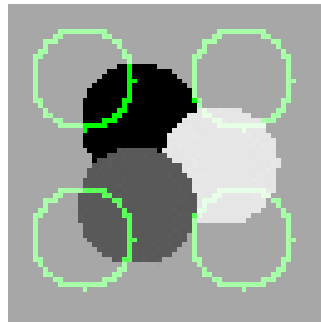
Unfortunately, the proposed method detects the small variations in the smooth regions if the target image is composed of only a few smooth regions. This defect, known as over-segmentation, is illustrated in Figure 3.19.



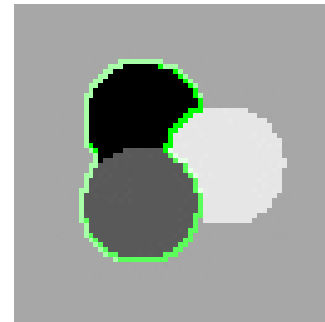
(a)



(b)



(c)



(d)

Figure 3.14: The hierarchical four-phase segmentation based on the approximate Mumford-Shah gradient flow method. Image size: 64×64 , $\mu_1 = \mu_2 = 0.0001 \times 255^2$, $\lambda_1 = \lambda_2 = 1$. (a) The synthetic image composed of three regions with two different mean values and the initial curves. (b) Segmentation result of (a). Computation time is 0.8 s. (c) The synthetic image composed of three regions with three different mean values and the initial curves belonging to the first step. (d) Segmentation result of the first step. Computation time is 0.6 s. (e) The initial curves belonging to the second step. (f) Segmentation result of the second step. Total computation time is 1.1 s.

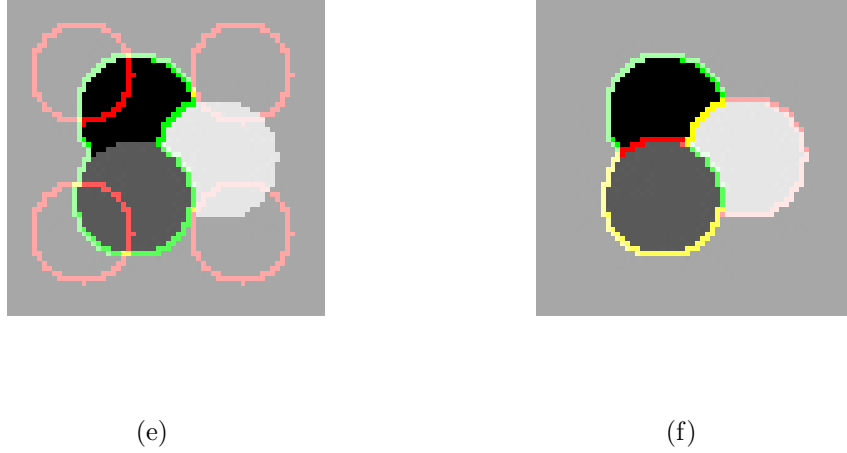


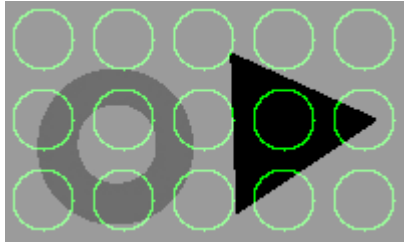
Figure 3.14: continued

3.2.4 Denoising After Segmentation

After getting the correct boundary localization, the denoising becomes a simple issue. In order not to lose the edge information, each denoising process is applied to inside and outside the zero level of evolving level set function ϕ but not across the zero level. This denoising process can be achieved with any of the diffusion filters given in Section 2.3 because of their high noise smoothing capability. For the segmentation using one level set function, the denoising takes place in two steps, i.e., one step for the regions $\phi > 0$ and the other step for $\phi < 0$. If two or more level set functions are used for the proper segmentation, 2^n smoothing steps are required, where n indicates the number of active level sets. The effects of the denoising by an anisotropic diffusion filter on the previously segmented images and the output SNR values are seen in Figure 3.20. The output SNRs are calculated using

$$SNR = 10 \log_{10} \left(\frac{\|u\|^2}{\|u_0 - u\|^2} \right) \quad (3.53)$$

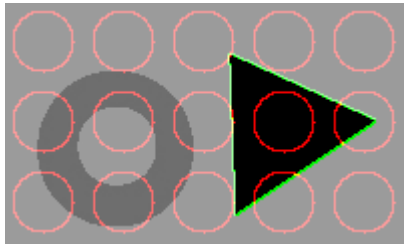
where u_0 and u are the original unnoisy image and the filtered image, respectively.



(a)



(b)

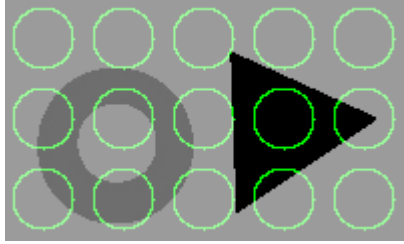


(c)



(d)

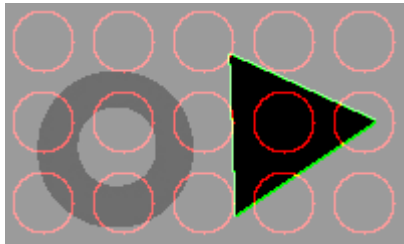
Figure 3.15: The hierarchical four-phase segmentation based on the approximate Mumford-Shah gradient flow method without the detection of the object boundary. Image size: 120×201 , $\mu_1 = \mu_2 = 0.0001 \times 255^2$, $\lambda_1 = \lambda_2 = 1$.



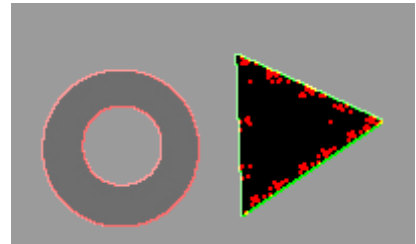
(a)



(b)

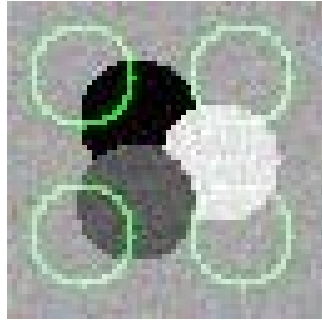


(c)

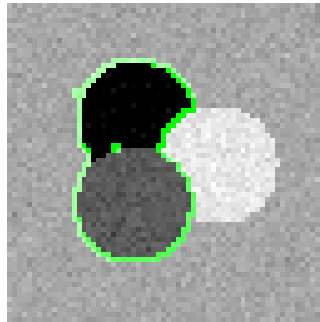


(d)

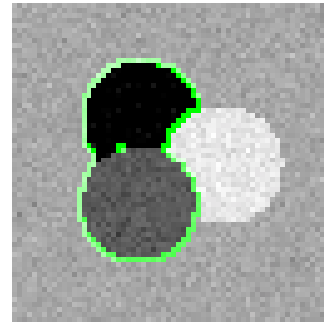
Figure 3.16: The hierarchical four-phase segmentation based on the approximate Mumford-Shah gradient flow method with the detection of the small variations in the homogeneous regions. Image size: 120×201 , $\mu_1 = \mu_2 = 0.0001 \times 255^2$, $\lambda_1 = \lambda_2 = 100000$.



(a)

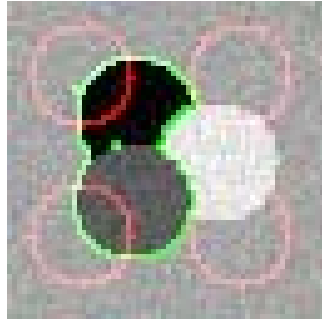


(b)

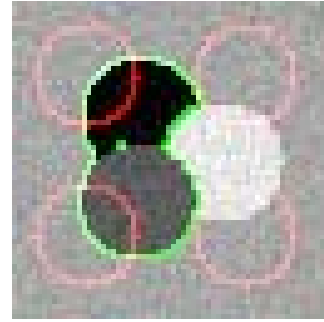


(c)

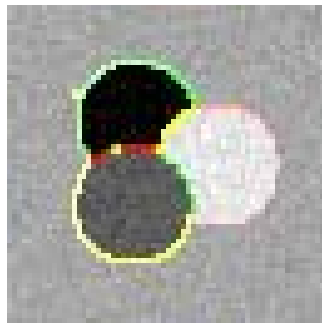
Figure 3.17: The hierarchical four-phase segmentations based on the Chan-Vese active contour method (left column) and the proposed method (right column). (a) 64 x 64 synthetic image with zero mean Gaussian white noise (SNR = 25dB) and the initial curves for the first step (b), (c) The results of the first steps. (b) $\mu_1 = 0.5\sigma^2 = 1484$, $\lambda_1 = 6$, (c) $\mu_1 = 0.0001 \times 255^2$, $\lambda_1 = 1$. Computation times are (b) 27.8 s, (c) 0.8 s. (d), (e) The initial curves for the second steps. (f), (g) The results of the second steps. $\mu_2 = 0.5\sigma^2 = 1484$, $\lambda_2 = 6$. Total computation times are (f) 43.7 s, (g) 12.5 s.



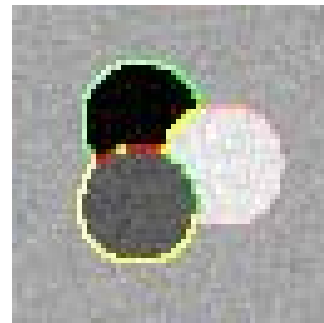
(d)



(e)



(f)



(g)

Figure 3.17: continued



(a)



(b)

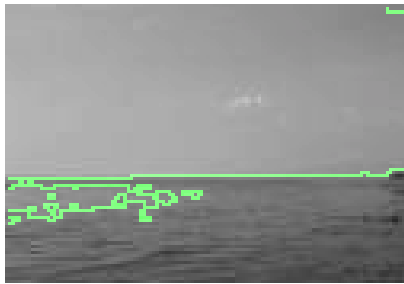


(c)

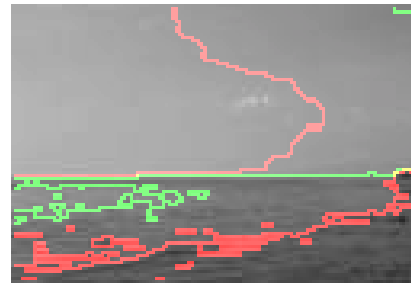
Figure 3.18: Segmentation of the well-known house image using the proposed hierarchical four-phase segmentation approach. (a) The original 256×256 test image. (b) The segmented image after the first segmentation step. $\mu_1 = 0.0001 \times 255^2$, $\lambda_1 = 1$. Computation time is 4.7 s. (c) The segmented image after the second segmentation step. $\mu_2 = 0.5\sigma^2 = 1059$, $\lambda_2 = 6$. Total computation time is 667.9 s.



(a)

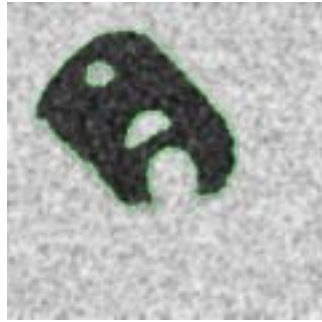


(b)



(c)

Figure 3.19: Over-segmentation of an image. (a) The original 126 x 87 test image. (b) The segmented image after the first segmentation step. $\mu_1 = 0.0001 \times 255^2$, $\lambda_1 = 1$. Computation time is 0.8 s. (c) The segmented image after the second segmentation step. $\mu_2 = 0.5\sigma^2 = 502.2$, $\lambda_2 = 6$. Total computation time is 53.3 s.



(a)



(b)

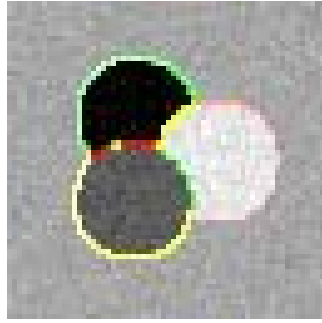


(c)

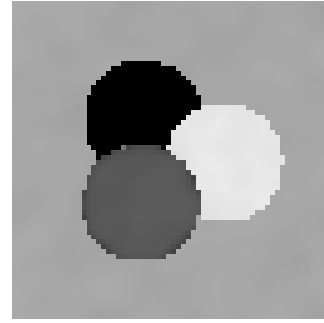


(d)

Figure 3.20: The effect of the anisotropic diffusion filtering on the previously segmented images. Left: The segmented noisy images. (a) Natural noise. The input SNRs are (c) 10 dB, (e) 25 dB. Right: Filtered images. The output SNRs are (d) 17.45 dB, (f) 35.55 dB.



(e)



(f)

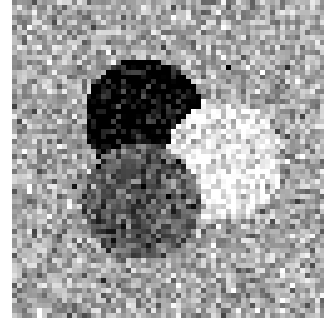
Figure 3.20: continued

3.2.5 Effects of Prefiltering

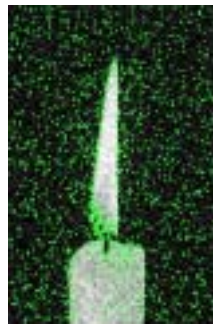
In the segmentation and denoising algorithm, the segmentation process which is sensitive to discontinuities in the images is run firstly. Unfortunately, in applications with low signal-to-noise ratio, the noisy spikes are regarded as the objects to be detected. In order to handle this problem, it is a good choice to implement a prefiltering scheme prior to segmentation. This prefiltering scheme has to smooth the noise in piecewise smooth regions of interest. On the contrary, its smoothing action must not take place across the edges. One of the proper filtering schemes satisfying these preliminaries is the nonlinear isotropic diffusion filter as explained previously. However, in the simulations, the blurring effect of nonlinear diffusion filtering is seen at some boundaries. Although the boundaries of the smooth parts are blurred, the desired boundary locations are found due to the efficiency of the segmentation algorithm. The suitability of the prefiltering issue can be observed in Figure 3.21.



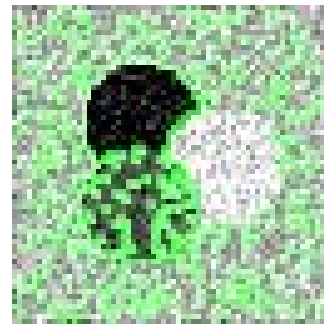
(a)



(b)



(c)

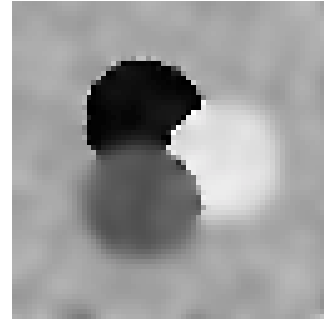


(d)

Figure 3.21: The effect of the prefiltering scheme for the segmentation and denoising of the very noisy images. The First Row: The original images with white Gaussian noise. The input SNRs are (a) 3 dB, (b) 13 dB. The Second Row: The unsatisfactory segmentations. The Third Row: The smoothed images after prefiltering. The Last Row: The filtered images after segmentation and denoising. The output SNRs are (g) 11.46 dB, (h) 23.1 dB.



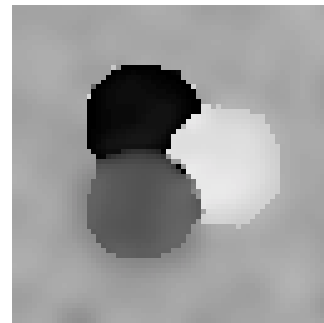
(e)



(f)



(g)



(h)

Figure 3.21: continued

3.3 Proposed Method

Combining the topics above, the steps for a fast and proper segmentation and denoising method is developed as:

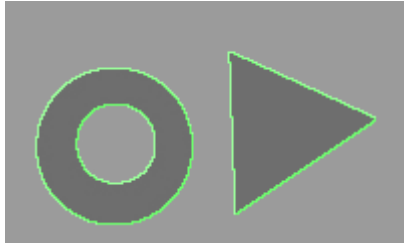
- A nonlinear diffusion filter is applied if necessary on the noisy image.
- The approximated Mumford-Shah gradient flow is applied to the image with automatic level set initialization. It is a good idea to select an initial ϕ whose zero level is composed of closed curves distributed on the image.
- Check whether the two-phase segmentation satisfies the expectations. If not, apply the second step of hierarchical segmentation by using the Chan-Vese active contour method.
- Finally, apply the anisotropic diffusion filtering in the segmented piecewise smooth regions independently in order not to cause blurring at the detected boundaries.

3.4 Comparison of the Proposed Method with the Normalized Cuts Method

The normalized cuts method is a widely used segmentation method proposed by Shi and Malik [19], [20]. In this method, the segmentation problem is taken as a graph partitioning problem, and a global criterion, called the normalized cut, is proposed for segmenting the graph. It groups the nodes forming the image according to a cost function which is a measure of the similarity among the nodes. The similarity is inversely proportional to the difference in color and position.

While using the normalized cuts method, the number of segments, e.g., the number of the observed smooth regions in the image, has to be set at the beginning. However, in some simulations this value might be insufficient for the proper segmentation. In this case, it has to be set to a larger value which can be

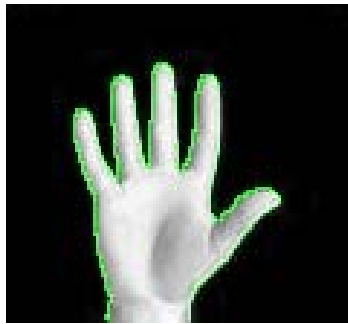
found by trial and error. In the following simulations, it is set to the minimum value which enables the boundaries of the observed smooth regions to be detected. In Figure 3.22, the segmentation results according to the proposed and normalized cuts methods are given in the left and right columns, respectively. The image on the first row is properly segmented by the two methods, where the proposed method is faster. The processed image in the second and the third rows is composed of two smooth regions. In the second row, the number of segments for the normalized cuts method is set to two, and it is observed that the method can not segment the image properly. In the third row, this number is increased to three. This time the normalized cuts method segments the image, detects the boundaries but includes an unexpected line in one of the smooth regions. In the fourth row, similar problems are encountered for the normalized cuts method while processing the image composed of four smooth regions. The number of segments for the normalized cuts method is set to six and unexpected lines are still observed on the processed image. Additionally, the detected boundaries for the normalized cuts method in the third and the fourth rows are not the exact ones surrounding the smooth regions while the proposed method detects them properly. For the segmentation results given in the fifth row, the second segmentation step of the proposed method is not activated. In this case, it segments the image faster than the normalized cuts method where the number of segments is set to five. However, the proposed method detects less boundaries than the normalized cuts method. For the segmentation results given in the last row, the second step of the proposed method is activated; and for the normalized cuts method the number of segments is set to twenty. In this case, the proposed method ends up with more boundary detection but slower segmentation than the normalized cuts method. According to these results, it can be concluded that the proposed method results in better image segmentation in the sense of boundary localization. Additionally, there is no need to set a parameter for the proper segmentation, and its computation time is less than that of the normalized cuts method for the cases where the first step of the proposed method is adequate for the proper segmentation.



(a)



(b)



(c)

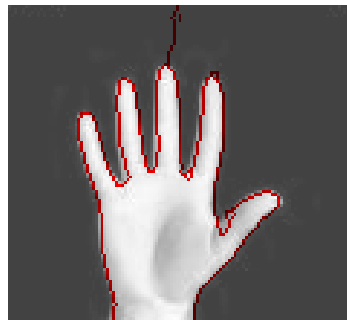


(d)

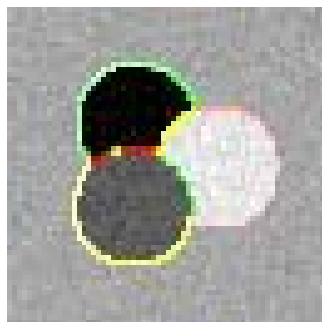
Figure 3.22: The segmentation results due to the proposed method (left column) and the normalized cuts method (right column). The corresponding computation times are (a) 2 s, (b) 28.3 s, (c) 0.4 s, (d) 10.8 s, (e) 0.4 s (f) 12.9 s, (g) 12.5 s, (h) 2.7s, (i) 0.4 s, (j) 15.7 s, (k) 401 s, (l) 77 s. The number of segments set at the beginning in the normalized cuts method are (b) 4, (d) 2, (f) 3, (h) 6, (j) 5 and (l) 20.



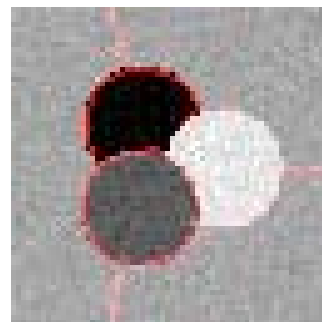
(e)



(f)



(g)



(h)



(i)

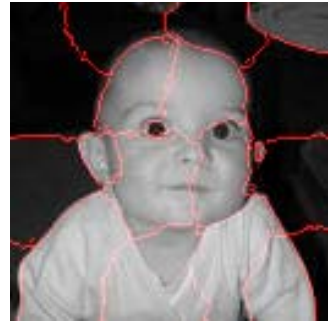


(j)

Figure 3.22: continued



(k)



(l)

Figure 3.22: continued

CHAPTER 4

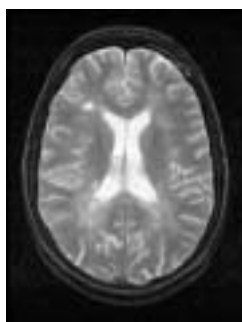
SIMULATIONS ON SOME APPLICATIONS

In the previous chapter, a fast and suitable segmentation and denoising method is introduced. However, the method have been generally applied on the synthetic images. In this chapter, the method is examined on some specific application areas, namely, medical imagery, thermal imaging and SAR imagery.

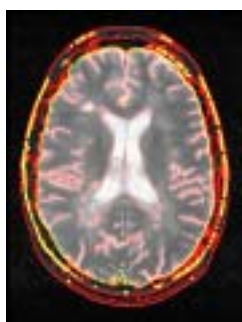
4.1 Simulations on Medical Imagery

The segmentation and denoising is a key issue in medical imagery in order to get the details from the medical images. By this way, some illnesses are diagnosed. As an illustration, the osteoarthritis can be diagnosed by observing the volumetric change in the cartilage in the knee. For the precise calculation of the area and the volume of the cartilage, a proper segmentation method has to be used. Due to these facts, active contours are widely used in medical imagery.

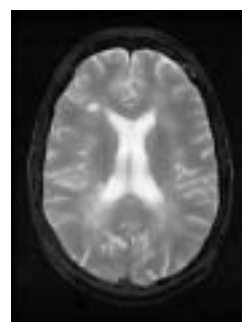
The segmentation and denoising method proposed in this work is applicable for various kinds of medical imagery including magnetic resonance imaging (MRI), computed tomography (CT), X-ray imaging and ultrasound. It eliminates the internal noise in the images and blurring defects. In Figure 4.1, the results of the proposed method on some MRI images are given.



(a)



(b)

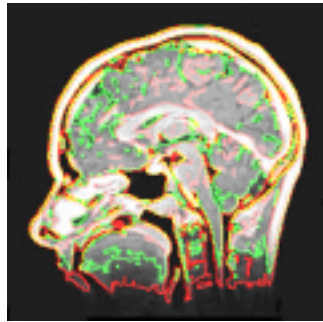


(c)

Figure 4.1: The segmentation and denoising of MRI images with the proposed method. Prefiltering scheme is not applied. (a), (d), (g) Original MRI images. (a) Image size: 256 x 192. (d) Image size: 182 x 182. (g) Image size: 182 x 182. (b), (e), (h) The segmented parts in the images. Computation times are (b) 212.7 s, (e) 217.2 s and (h) 103.9 s. (c), (f), (i) Filtered MRI images.



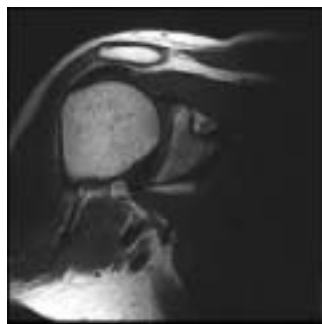
(d)



(e)

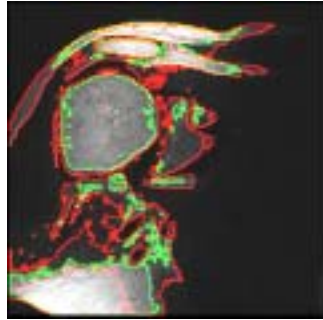


(f)

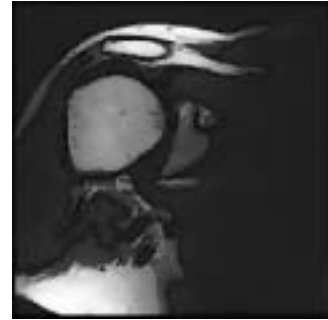


(g)

Figure 4.1: continued



(h)



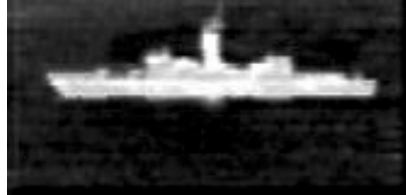
(i)

Figure 4.1: continued

4.2 Simulations on Thermal Imaging

Thermal imaging makes it possible to see the objects in daylight or night by detecting the infrared emission from the objects based on their temperature. The amount of radiation emitted by an object increases with temperature, therefore thermal imaging allows one to see variations in temperature.

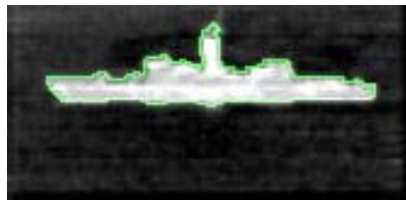
The heat flow according to the temperature of the objects also warms or cools their environment; therefore, the objects are blurred in the infrared images. Additionally, some defects in the infrared images due to the improper normalization of the infrared sensor responses can be seen. These problems are dealt with the proposed method in this work. Some illustrations to thermal imaging applications of the proposed method are given in Figure 4.2. According to these results, it is observed that the edges of the smooth regions become sharper and the details of the objects are more visible.



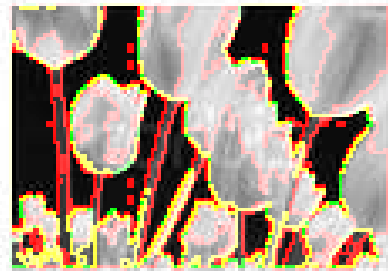
(a)



(b)



(c)



(d)

Figure 4.2: The segmentation and denoising of infrared images with the proposed method. Prefiltering scheme is not applied. (a), (b) Original infrared images. (a) Image size: 80 x 166. (b) Image size: 89 x 120. (c), (d) The segmented parts in the images. (c) Only one level set function is applied. Computation times are (c) 1.6 s and (d) 14.1 s. (e), (f) Filtered infrared images.



(e)



(f)

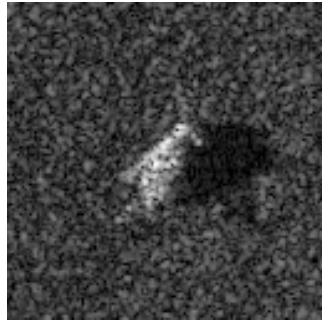
Figure 4.2: continued

4.3 Simulations on SAR Imagery

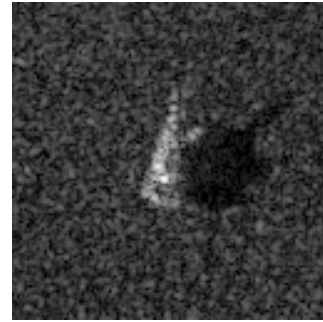
Synthetic Aperture Radar (SAR) is a microwave instrument that produces high-resolution imagery of the Earth's surface in all weather conditions. It differs from normal cameras in that it provides its own illuminating light at radio wavelengths, and each pixel takes the value according to the energy of the backscatter of the transmitted signal. The darker part in the SAR image represents the low backscatter, and the brighter parts represent the high backscatter. The level of backscatter for a target area depends on some factors such as the smoothness of the target area, polarization of the pulses, moisture in the target area, etc. The detailed information on SAR imagery is given in [7].

The radar images are composed of many dots due to the non-smooth radar backscatter representing each pixel value. Since, multiplicative speckle noise is observed in SAR images due to the scattering phenomena, a preprocessing scheme which involves logarithmic transform in order to convert the multiplicative noise to additive noise is required. In this work, SAR images are processed

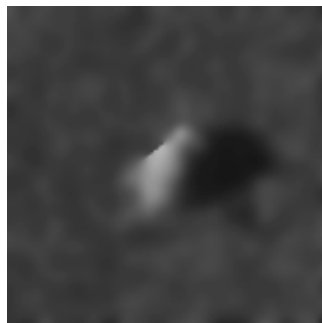
by the proposed method after the logarithmic preprocessing scheme. However, the signal-to-noise ratio still remains low after it. Therefore, the prefiltering scheme with a nonlinear diffusion filter is activated in the simulations. The results of SAR image processing by the proposed method is given in Figure 4.3.



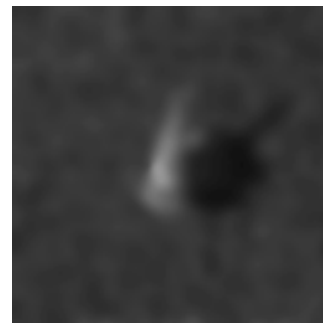
(a)



(b)

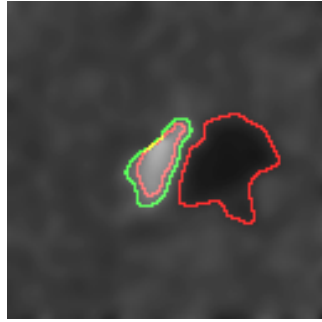


(c)

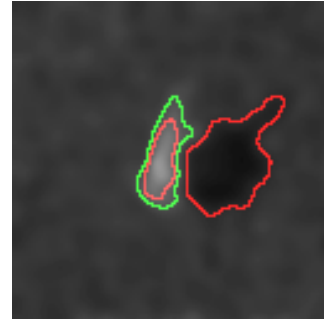


(d)

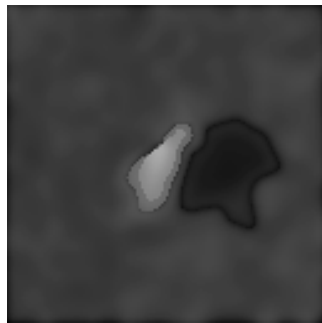
Figure 4.3: The segmentation and denoising of SAR images with the proposed method. (a), (b) Original SAR images. Image size: 128 x 128 (c), (d) The denoised images after prefiltering. (e), (f) The segmented parts in the images. Computation times are (e) 34.2 s and (f) 30.1 s. (g), (h) Filtered SAR images.



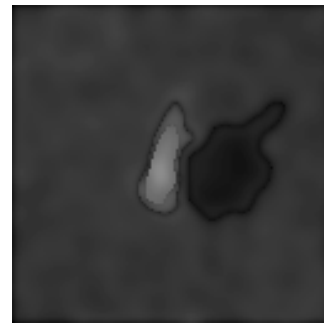
(e)



(f)



(g)



(h)

Figure 4.3: continued

CHAPTER 5

CONCLUSION

In this thesis, the variational methods on image segmentation and denoising problem have been examined. These methods are the approximate solutions to the variational problem of minimizing the functional presented in Mumford-Shah model. Using the results of these methods, a fast and robust image segmentation and denoising algorithm has been proposed. The algorithm differs from the one developed by Gao and Bui in that the hierarchical segmentation part is composed of two different segmentation methods, namely the approximate Mumford-Shah gradient flow method and the Chan-Vese active contour method, and a prefiltering process has been added in order to deal with very noisy images.

While constructing the algorithm, some comparisons have been made on the segmentation methods which have been implemented via the level set methods. The results of the two methods have been found the same. However, it has been observed that the approximate Mumford-Shah gradient flow method results in faster convergence of the evolving curve to the boundaries of the piecewise smooth regions. In order to decrease the convergence time for the Chan-Vese active contour method, the initialization process has been made automatic, which embeds an initial level set function whose zero level is composed of the closed curves crossing the image plane regularly. In spite of this modification, the Chan-Vese active contour method has remained much slower than the other one. The reason is that the approximate Mumford-Shah gradient flow has a more globally effective minimizer due to its multiplicative term, i.e., the gradient of the evolving level set function.

During the experimental work, it has been seen that the two-phase segmentation has not satisfied the expectations even in simple synthetic images.

Depending on the approaches presented in [24] and [8], the hierarchical segmentation approach where the second segmentation step uses the results of the first one has been chosen in order to segment the bulk of the homogeneous parts in the image. When the hierarchical approach has been formed by running the approximate Mumford-Shah flow in two consecutive steps, the unsatisfactory segmentation of small variations in the homogeneous parts has been observed. When the Chan-Vese active contour method was used in a similar way, the hierarchical segmentation process has been found to be long-running due to the first segmentation step. Based on these facts, a fast hierarchical segmentation algorithm has been proposed by running the Chan-Vese active contour method just after the approximate Mumford-Shah gradient flow method.

After the boundaries of the noisy regions were detected, a diffusion filter has been applied to the each segmented region independently. By this way, the edges of the homogeneous regions have been preserved, and the signal-to-noise ratio of the image has been increased.

The segmentation and denoising algorithm works fine for low noisy images. Unfortunately, the noise particles in the smooth regions are also detected in very noisy applications. This problem has been handled by modifying the scaling parameters in the update term of the level set function up to a point. In order to obtain a generalized solution, a prefiltering process which uses the nonlinear diffusion filter as the edge-preserved denoising filter has been added.

The experimental work has shown the effectiveness of the proposed segmentation method. Compared with the normalized cuts method, it has resulted in better boundary localization. However, the proposed method could not process the texture images, because the similarities and dissimilarities among the regions are not considered in the segmentation steps. The proposed method has been tested for the applications such as medical imagery, thermal imaging and SAR imagery, and satisfactory results have been obtained. The edges of the smooth regions in the images have been detected and the blurring effects have been eliminated.

During the simulations, it has been observed that the selection of the appropriate scaling parameters has affected the convergence time of the segmentation

methods and the sizes of the segmented regions. It is a good idea to make the selection of them automatically depending on the image. In addition to that, unexpected results in the four-phase hierarchical segmentation approach based on the approximated Mumford-Shah gradient flow method have been detected. If the reasons of this problem are found and they are eliminated, then a faster segmentation approach can be obtained. These topics will be the subject for the future work.

APPENDIX A

FIRST VARIATION AND EULER-LAGRANGE EQUATION

Minimization paradigm is an inevitable process in order to find solutions to the mathematical models of systems in daily life. One of the basic mathematical analysis of nonlinear minimization process on infinite dimensional function spaces is known as the calculus of variations. It can be used to find an unknown function that minimizes or maximizes a functional which is a mapping of the functions in a function space to another one.

The simplest functional to be minimized is the one which depends upon at most the first derivative of a continuous and scalar function. $y = u(x) \in C^1[a, b]$ is the suitable function to be determined which minimizes the functional

$$J[u] = \int_a^b L(x, u, u') dx \quad (\text{A.1})$$

where the integrand is known as the Lagrangian for the variational problem and u' is the first derivative of u . The gradient of the functional of minimizer u vanishes, i.e., $\nabla J[u] = 0$, and it is defined by the directional derivative formula

$$\langle \nabla J[u], \delta u \rangle = \left. \frac{d}{dt} J[u + t\delta u] \right|_{t=0} \quad (\text{A.2})$$

where δu is the function which indicates the direction of the computed derivative. δu and the gradient operator on functionals are known as the variation in the function u and the variational derivative, respectively. In (A.2), the standard inner product defined in L^2 space,

$$\langle f, g \rangle = \int_a^b f(x)g(x) dx, \quad (\text{A.3})$$

is used. Substituting (A.2) to (A.1), and by the chain rule,

$$\begin{aligned} \frac{d}{dt}J[u + tv] &= \int_a^b \frac{d}{dt}L(x, u + tv, u' + tv')dx \\ &= \int_a^b \left[v \frac{\partial L}{\partial u}(x, u + tv, p + tv') + v' \frac{\partial L}{\partial p}(x, u + tv, p + tv') + v' \right] dx \end{aligned} \quad (\text{A.4})$$

is obtained where p is the first derivative of $u(x)$, i.e., u' and $v = \delta u$. Setting $t = 0$, (A.4) is simplified to

$$\langle \nabla J[u], v \rangle = \int_a^b \left[v \frac{\partial L}{\partial u}(x, u, p) + v' \frac{\partial L}{\partial p}(x, u, p) \right] dx. \quad (\text{A.5})$$

In literature, the integral part in (A.5) is known as the first variation of the functional $J[u]$.

Defining a new function

$$r(x) = \frac{\partial L}{\partial p}(x, u(x), p(x)), \quad (\text{A.6})$$

the second term on the right-hand side of (A.5) can be found by integrating by parts as

$$\int_a^b r(x)v'(x)dx = [r(b)v(b) - r(a)v(a)] - \int_a^b r'(x)v(x)dx \quad (\text{A.7})$$

where

$$r'(x) = \frac{d}{dx} \left(\frac{\partial L}{\partial p}(x, u, p) \right) = \frac{\partial^2 L}{\partial x \partial p}(x, u, p) + p \frac{\partial^2 L}{\partial u \partial p}(x, u, p) + p' \frac{\partial^2 L}{\partial p^2}(x, u, p). \quad (\text{A.8})$$

The boundary conditions on the minimizer function $u(x)$ and $u(x) + tv(x)$ are the same. Thus, $v(x)$ satisfies the homogeneous boundary conditions

$$v(a) = 0 \quad \text{and} \quad v(b) = 0. \quad (\text{A.9})$$

Finally,

$$\langle \nabla J[u], v \rangle = \int_a^b \nabla J[u]v dx = \int_a^b v \left[\frac{\partial L}{\partial u}(x, u, p) - \frac{d}{dx} \left(\frac{\partial L}{\partial p}(x, u, p) \right) \right] dx \quad (\text{A.10})$$

is obtained since the boundary terms in (A.7) vanish. Inspecting (A.10), it is concluded that the minimizer $u(x)$ should satisfy

$$\nabla J[u] = \frac{\partial L}{\partial u}(x, u, p) - \frac{d}{dx} \frac{\partial L}{\partial p}(x, u, p) = 0. \quad (\text{A.11})$$

Using (A.8), a second order differential equation,

$$E(x, u, p, p') = \frac{\partial L}{\partial u}(x, u, p) - \frac{\partial^2 L}{\partial x \partial p}(x, u, p) - u' \frac{\partial^2 L}{\partial u \partial p}(x, u, p) - p' \frac{\partial^2 L}{\partial p^2}(x, u, p) = 0, \quad (\text{A.12})$$

for the minimizer is obtained. This equation is the Euler-Lagrange equation associated with (A.1).

APPENDIX B

CURVATURE

Curvature is a frequently used notion in applications requiring curve evolution and it simply associates the rate of turning of the tangential vector in terms of the normal vector on the moving curve. It is defined for parameterized curves and curves as an isolevel of a function. Curvature of a curve is given in Figure B.1.

B.1 Curvature of the Parameterized Curves

Let $\vec{r}(p)$ be a parameterized curve, $\vec{r}(p) = (r_1(p), r_2(p))$, in \mathbb{R}^2 where $0 \leq p \leq 1$. Then the unit tangential vector $\vec{T}(p)$ at $\vec{r}(p)$ and the unit normal vector $\vec{N}(p)$ at $\vec{r}(p)$ can be written as

$$\vec{T}(p) = \frac{\vec{r}'(p)}{|\vec{r}'(p)|} = \left(\frac{r_1'(p)}{\sqrt{(r_1'(p))^2 + (r_2'(p))^2}}, \frac{r_2'(p)}{\sqrt{(r_1'(p))^2 + (r_2'(p))^2}} \right), \quad (\text{B.1})$$

$$\vec{N}(p) = \left(-\frac{r_2'(p)}{\sqrt{(r_1'(p))^2 + (r_2'(p))^2}}, \frac{r_1'(p)}{\sqrt{(r_1'(p))^2 + (r_2'(p))^2}} \right) \quad (\text{B.2})$$

where $\vec{r}'(p)$ is the first derivative of $\vec{r}(p)$ with respect to p . The arc-length parametrization of curve \vec{C} is given as $\vec{r}(s)$ where

$$s(p) = \int_0^p \sqrt{(r_1'(\tau))^2 + (r_2'(\tau))^2} d\tau. \quad (\text{B.3})$$

It can be shown that the rate of turning of tangential vector is collinear to the normal vector, i.e.,

$$\frac{1}{|\vec{r}'(s)|} \frac{\partial}{\partial s} \left(\frac{\vec{r}'(s)}{|\vec{r}'(s)|} \right) = \kappa(s) \vec{N}(s). \quad (\text{B.4})$$

The linearizing term $\kappa(s)$ is named as the curvature of \vec{C} at point $r(s)$ and

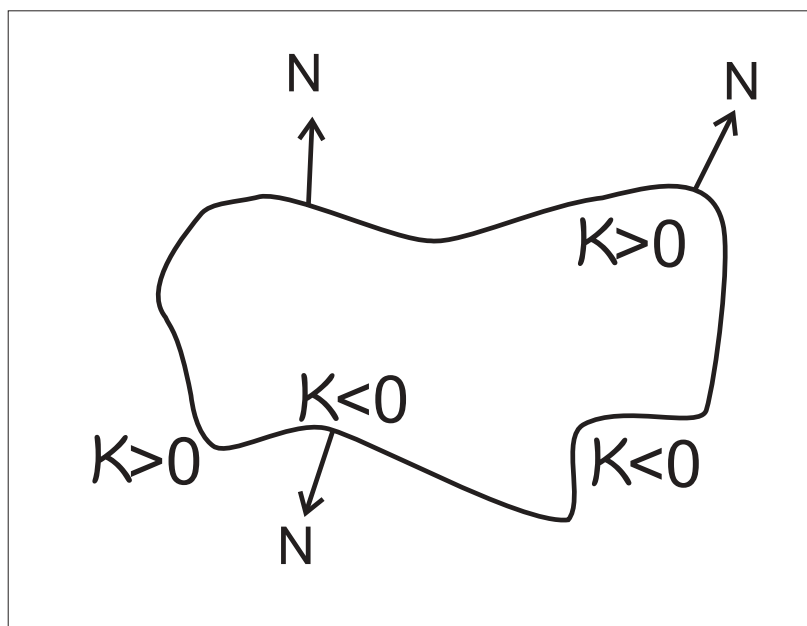


Figure B.1: Curvature of a curve.

calculated as

$$\kappa(s) = \frac{r_1'(s)r_2''(s) - r_1''(s)r_1'(s)}{((r_1'(s))^2 + (r_2'(s))^2)^{\frac{3}{2}}}. \quad (\text{B.5})$$

B.2 Curvature of the Curves as Isolevels of a Function

Let $\vec{r}(s)$ be the k -level of a function $\phi : \mathbb{R}^2 \rightarrow \mathbb{R}$, i.e.,

$$\vec{r}(s) = \{(r_1(s), r_2(s)); \quad \phi(r_1(s), r_2(s)) = k\}. \quad (\text{B.6})$$

Differentiating the conditional equality for $\vec{r}(s)$ with respect to s ,

$$r_1'(s)\phi_{r_1} + r_2'(s)\phi_{r_2} = 0 \quad (\text{B.7})$$

is obtained. There exists a constant λ such that

$$\begin{aligned} r_1'(s) &= -\lambda\phi_{r_2}, \\ r_2'(s) &= \lambda\phi_{r_1}, \end{aligned} \quad (\text{B.8})$$

is satisfied. Differentiating (B.7) with respect to s and using the relationship given in (B.8),

$$\lambda^2((\phi_{r_1})^2\phi_{r_2}^2 + (\phi_{r_2})^2\phi_{r_1}^2 - 2\phi_{r_1}\phi_{r_2}\phi_{r_1r_2}) + \frac{1}{\lambda}(r_1''r_2' - r_2''r_1') = 0 \quad (\text{B.9})$$

is obtained. Since $\vec{r}'(s) = (r_1'(s), r_2'(s))$ is the unit tangential vector, the relation between λ and ϕ is found as

$$\lambda^2 = \frac{1}{|\nabla\phi|^2}. \quad (\text{B.10})$$

Substituting (B.5) and (B.10) in (B.9), the curvature of the curve $\vec{r}(s)$ which is an isolevel of ϕ is emerged as

$$\kappa = \frac{(\phi_{r_1})^2\phi_{r_2}^2 + (\phi_{r_2})^2\phi_{r_1}^2 - 2\phi_{r_1}\phi_{r_2}\phi_{r_1r_2}}{((\phi_{r_1})^2 + (\phi_{r_2})^2)^{3/2}}. \quad (\text{B.11})$$

The simplified version is obtained as

$$\kappa = \text{div}\left(\frac{\nabla\phi}{|\nabla\phi|}\right). \quad (\text{B.12})$$

APPENDIX C

FLUX MAXIMIZING FLOW

Total inward flux of a vector field \vec{F} through a closed curve \vec{C} is formulated as

$$\mathcal{K} = \oint_{\vec{C}} \langle \vec{F}, \vec{N} \rangle ds \quad (\text{C.1})$$

where \vec{N} is the unit inward normal vector of \vec{C} . Let $\vec{C} = \vec{C}(p, t)$ be a family of closed curves where t parameterizes the family and p parameterizes the curve where $0 \leq p \leq 1$. Since the curve is closed and smooth, $\vec{C}(0, t) = \vec{C}(1, t)$ and $\frac{\partial \vec{C}}{\partial t}(p, t)|_{p=0} = \frac{\partial \vec{C}}{\partial t}(p, t)|_{p=1}$.

The relation between the infinitesimal arc-length term ds in (C.1) and its parameterized version dp is given by

$$ds = \|\vec{C}_p\| dp. \quad (\text{C.2})$$

Embedding this result with the variable t to (C.1), the time dependent parameterized form of (C.1) is written as

$$\mathcal{K}(t) = \int_0^1 \langle \vec{F}, \vec{N} \|\vec{C}_p\| \rangle dp. \quad (\text{C.3})$$

$\vec{N} \|\vec{C}_p\|$ and \vec{C}_p have the same magnitude and they are perpendicular to each other. The transformation

$$\vec{N} \|\vec{C}_p\| = \mathcal{T} \vec{C}_p \quad (\text{C.4})$$

relates them and simplifies the further calculations. The transformation matrix \mathcal{T} is the 90 degree rotation matrix defined by

$$\mathcal{T} = \begin{bmatrix} 0 & 1 \\ -1 & 0 \end{bmatrix}. \quad (\text{C.5})$$

The next step is differentiating the time varying total flux calculating equation (C.3) with respect to t , integrating by parts, which establishes (C.6). It has to

be noted that a simplification is made based on the fact that the derivative of the closed curves at the boundaries are equal to each other in order to obtain (C.6).

$$\begin{aligned}\frac{\partial \mathcal{K}(t)}{\partial t} &= \int_0^1 (\langle \vec{F}_t, \mathcal{T} \vec{C}_p \rangle + \langle \vec{F}, \mathcal{T} \vec{C}_{pt} \rangle) dp \\ &= \int_0^1 (\langle \vec{F}_t, \mathcal{T} \vec{C}_p \rangle - \langle \vec{F}_p, \mathcal{T} \vec{C}_t \rangle) dp.\end{aligned}\quad (\text{C.6})$$

By chain rule, \vec{F}_t and \vec{F}_p is derived as

$$\begin{aligned}\vec{F}_t &= \begin{bmatrix} \frac{\partial F_1}{\partial x} \frac{\partial x}{\partial t} + \frac{\partial F_1}{\partial y} \frac{\partial y}{\partial t} \\ \frac{\partial F_2}{\partial x} \frac{\partial x}{\partial t} + \frac{\partial F_2}{\partial y} \frac{\partial y}{\partial t} \end{bmatrix} \\ &= (\mathcal{D} \vec{F}) \vec{C}_t,\end{aligned}\quad (\text{C.7})$$

$$\begin{aligned}\vec{F}_p &= \begin{bmatrix} \frac{\partial F_1}{\partial x} \frac{\partial x}{\partial p} + \frac{\partial F_1}{\partial y} \frac{\partial y}{\partial p} \\ \frac{\partial F_2}{\partial x} \frac{\partial x}{\partial p} + \frac{\partial F_2}{\partial y} \frac{\partial y}{\partial p} \end{bmatrix} \\ &= (\mathcal{D} \vec{F}) \vec{C}_p.\end{aligned}\quad (\text{C.8})$$

where D is the 2x2 Jacobian matrix. Combining the equations (C.6), (C.7) and (C.8) together and doing some manipulations such as rearrangements and simplifications on the combined structure,

$$\begin{aligned}\frac{\partial \mathcal{K}(t)}{\partial t} &= \int_0^1 \langle (\mathcal{D} \vec{F}) \vec{C}_t, \mathcal{T} \vec{C}_p \rangle - \langle (\mathcal{D} \vec{F}) \vec{C}_p, \mathcal{T} \vec{C}_t \rangle dp \\ &= \int_0^1 \langle \vec{C}_t, \left[(\mathcal{T}^T (\mathcal{D} \vec{F}))^T - (\mathcal{T}^T (\mathcal{D} \vec{F})) \right] \vec{C}_p \rangle dp \\ &= \int_0^1 \left\langle \vec{C}_t, \left(\begin{bmatrix} -\frac{\partial F_2}{\partial x} & \frac{\partial F_1}{\partial x} \\ -\frac{\partial F_2}{\partial y} & \frac{\partial F_1}{\partial y} \end{bmatrix} - \begin{bmatrix} -\frac{\partial F_2}{\partial x} & -\frac{\partial F_2}{\partial y} \\ \frac{\partial F_1}{\partial x} & \frac{\partial F_1}{\partial y} \end{bmatrix} \right) \vec{C}_p \right\rangle dp \\ &= \int_0^1 \left\langle \vec{C}_t, \left(\left(\frac{\partial F_1}{\partial x} + \frac{\partial F_2}{\partial y} \right) \begin{bmatrix} 0 & 1 \\ -1 & 0 \end{bmatrix} \right) \vec{C}_p \right\rangle dp \\ &= \int_0^1 \langle \vec{C}_t, (\nabla \cdot \vec{F}) \mathcal{T} \vec{C}_p \rangle dp\end{aligned}\quad (\text{C.9})$$

is attained. Using the predefined relation (C.2), (C.9) is reorganized as

$$\begin{aligned}\frac{\partial \mathcal{K}(t)}{\partial t} &= \int_0^1 \langle \vec{C}_t, (\nabla \cdot \vec{F}) \vec{N} \rangle \|\vec{C}_p\| dp \\ &= \oint_{\vec{C}} \langle \vec{C}_t, (\nabla \cdot \vec{F}) \vec{N} \rangle ds.\end{aligned}\quad (\text{C.10})$$

As a result, the total inward flux through a closed curve increases most rapidly by moving the each point of the curve in the inward normal vector direction with a magnitude of divergence of the vector field,

$$\vec{C}_t = (\nabla \cdot \vec{F}) \vec{N}. \quad (\text{C.11})$$

REFERENCES

- [1] Alvarez, L., Lions, P.L., Morel, J.M. "Image selective smoothing and edge detection by nonlinear diffusion II" *SIAM J. Numer. Anal.*, Vol. 29, no. 3, pp. 845-866, 1992.
- [2] Ambrossio, L., Tortorelli, V.M. "Approximation of functionals depending on jumps by elliptic functionals via Γ -convergence" *Comm. Pure Appl. Math.*, Vol. 43, no. 8, 1990.
- [3] Caselles, V., Kimmel, R., Sapiro, G. "Geodesic active contour models" *Inter. Journal Comp. Vision*, Vol. 22, pp. 61-79, 1997.
- [4] Catte, F., Lions, P.L., Morel, J.M., Coll, T. "Image selective smoothing and edge detection by nonlinear diffusion" *SIAM J. Numer. Anal.*, Vol. 29, no. 1, pp. 182-193, 1992.
- [5] Chan, T.F., Vese, L. "Active contours without edges" *IEEE Trans. Image Process.*, Vol. 10, No. 2, pp. 266 - 277, Feb. 2001.
- [6] Evans, L.C., Gariepy, R.F. "Measure theory and fine properties of functions" *CRC Press: Boca Raton, FL*, 1992.
- [7] Freeman, T. "What is imaging radar?" *www.southport.jpl.nasa.gov*, Jan. 1996.
- [8] Gao, S., Bui, T.D. "Image segmentation and selective smoothing by using Mumford-Shah model " *IEEE Trans. Image Process.*, Vol. 14, No. 10, pp. 1537 - 1549, Oct. 2005.
- [9] Kass, M., Witkin, A., Terzopoulos, D. "Snakes: Active contour models" *Inter. Journal Comp. Vision*, Vol. 1, pp. 321-331, 1988.
- [10] Mumford, D., Shah, J. "Optimal approximation by piecewise smooth functions and associated variational problems " *Comm. Pure Appl. Math.*, Vol. 42, pp. 577 - 685, 1989.

- [11] Osher, S., Sethian, J.A. "Fronts propagation with curvature dependent speed: Algorithms based on Hamilton-Jacobi formulations" *Journal Comp. Physics*, Vol. 79, pp. 12-49, 1988.
- [12] Osher, S., Fedkiw, R. "Level set methods and dynamic implicit surfaces" *Applied Math. Sciences*, Vol. 153, 2000.
- [13] Osher, S., Paragios, N. "Geometric level set methods in imaging, vision, and graphics" *Springer*, 2003.
- [14] Perona, P., Malik, J. "Scale-space and edge detection using anisotropic diffusion" *IEEE Trans. Pattern Anal. Machine Intel.*, Vol. 12, No. 7, pp. 1169-1186, July 1990.
- [15] Richardson, T.J. "Ph.D. dissertation" *Dept. Elect. Eng. Comp. Science, M.I.T.*, 1989.
- [16] Rudin, L., Osher, S., Fatemi, E. "Nonlinear total variation based noise removal algorithms" *Phys. D*, Vol. 60, pp. 259-268, 1992.
- [17] Schneider, M.K., Fieguth, P.W., Karl, W.C., Willsky, A. "Multiscale methods for the segmentation and reconstruction of signals and images" *IEEE Trans. Image Process.*, Vol. 9, No. 3, pp. 456-468, March 2000.
- [18] Sethian, J.A. "Level set methods and fast marching methods: Evolving interfaces in computational geometry, fluid mechanics, computer vision, and materials science" *Cambridge U.K: Cambridge Univ.Press*, 2nd Edition, 1999.
- [19] Shi, J., Malik, J. "Normalized cuts and image segmentation" *IEEE Conf. Computer Vision and Pattern Recogn.*, pp. 731-737, June 1997.
- [20] Shi, J., Malik, J. "Normalized cuts and image segmentation" *IEEE Trans. Pattern Anal. Machine Intel.*, Vol. 22, No. 8, pp. 888-905, Aug. 2000.
- [21] Tsai, A. "Curve evolution and estimation-theoretic techniques for image processing" *Ph.D. Dissertation to Harvard-M.I.T. Division of Health Sciences and Technology*, Aug. 2000.

- [22] Tsai, A., Yezzi, A., Willsky, A. "Curve evolution implementation of the Mumford-Shah functional for image segmentation, denoising, interpolation, and magnification " *IEEE Trans. Image Process.*, Vol. 10, No. 8, pp. 1169-1186, Aug. 2001.
- [23] Vasilevskiy, A., Siddiqi, K., "Flux maximizing geometric flows " *IEEE Trans. Pattern Anal. Machine Intel.*, Vol. 24, No. 12, pp. 1565 - 1578, Dec. 2002.
- [24] Vese, L., Chan, T.F. "A multiphase level set framework for image segmentation using the Mumford and Shah model " *Inter. Journal Comp. Vision*, Vol. 50, No. 3, pp. 271 - 293, July 2002.
- [25] Weickert, J. "Theoretical foundations of anisotropic in image processing" *Comput. Suppl.*, Vol. 11, pp. 221-236, 1996.
- [26] Weickert, J. "Anisotropic diffusion in image processing" *Stuttgart, Germany: Taeubner*, 1998.
- [27] Weickert, J., Schnör, C. "PDE-based preprocessing of meical images" *Künstliche Intell.*, Vol. 3, pp. 5-10, 2000.
- [28] Yezzi, A., Kichenassamy, S., Kumar, A., Olver, P., Tannenbaum, A. "A geometric snake model for segmentation of medical imagery" *IEEE Trans. Medical Imaging*, Vol. 16, No. 2, pp. 199-209, April 1997.
- [29] Yezzi, A., Tsai, A., Willsky, A. "Afully global approach to image segmentation via coupled curve evolution equations" *Journal Visual Comm. Image Repr.*, Vol. 13, pp. 195 - 216, 2002.
- [30] Zhao, H.K., Chan, T.F., Merriman, B., Osher, S. "A variational level set approach to multiphase motion" *Journal Comp. Physics*, Vol. 127, No. 167, pp. 179 - 195, Feb. 1996.